



Multiscale modeling of transport mechanisms, strain, and stress in bananas during drying

Fidele M. Abedi, Yuxiang Liu & Pawan S. Takhar

To cite this article: Fidele M. Abedi, Yuxiang Liu & Pawan S. Takhar (2024) Multiscale modeling of transport mechanisms, strain, and stress in bananas during drying, *Drying Technology*, 42:3, 540-562, DOI: [10.1080/07373937.2023.2280912](https://doi.org/10.1080/07373937.2023.2280912)

To link to this article: <https://doi.org/10.1080/07373937.2023.2280912>



Published online: 21 Nov 2023.



Submit your article to this journal [↗](#)



Article views: 74



View related articles [↗](#)



View Crossmark data [↗](#)



Multiscale modeling of transport mechanisms, strain, and stress in bananas during drying

Fidele M. Abedi^a, Yuxiang Liu^b, and Pawan S. Takhar^a

^aFood Science and Human Nutrition, University of Illinois at Urbana-Champaign, Urbana, IL, USA; ^bMechanical and Materials Engineering, Worcester Polytechnic Institute, Worcester, MA, USA

ABSTRACT

The two-scale Hybrid Mixture Theory-based mass balance and momentum balance equations, the multiscale energy balance equation, and the viscoelastic stress equation were solved to obtain the moisture, temperature, strain, and stress distributions during bananas' convective drying. The model was validated against experimental average moisture contents (mean absolute errors (MAEs): 0.022–0.121 g/g solids), center and near-the-surface temperatures (MAEs: 0.6–7.7 °C), and volumetric strain (MAEs: 0.06–0.13). The model was then used to evaluate the effectiveness of the fan on/off strategy in reducing stress cracking compared to continuous drying. Simulation results of axial stress gradients and experimental results of global crack indices using a 5-point hedonic scale showed that the fan on/off strategy effectively reduced stress cracking compared to continuous drying. Thus, drying bananas at 60 °C by turning the fan on and off intermittently can be applied to reduce stress cracking in the product while requiring only 1.76% more energy compared to continuous drying.

ARTICLE HISTORY

Received 14 December 2022
Revised 3 November 2023
Accepted 4 November 2023

KEYWORDS

Drying; stress; strain; stress-cracking; multiscale modeling; hybrid mixture theory

1. Introduction

Banana production boomed between 2008 and 2017, increasing by 15.35% and reaching 113.92 million metric tons in 2017^[1]. Although most of the production is traded and consumed fresh, interest in processing has grown manifold, and excellent potential for new products exists^[2]. Examples of processed products include dried or fried chips, flour, starch, and fruit bars^[1]. For many of these processed products, drying is an essential unit operation. However, drying results, in some cases, in stress-cracked or broken materials that are generally undesirable for consumer acceptance of many foods. Cracked and broken materials can also lead to insect infestation and microbial contamination^[3]. Therefore, attempts to decrease cracked and broken materials during drying have received considerable attention from research and industry communities.

However, tuning the process parameters to reduce stress cracking predictably requires knowledge of the spatiotemporal distribution of strain and stress during drying. Such knowledge can only be obtained by using appropriately designed experiments and accurate heat and mass transfer models in tandem. Stress-cracking

and breakage of food materials during drying are complex and result from the contribution and interaction of various factors. Some factors, such as spatial variation in material properties and heterogeneity in the porous matrix, are related to the matrix. Other factors, such as shrinkage and swelling, the stress of the flowing fluid over the solid matrix, thermal fluctuations, hydration stress at the solid/fluid interface, and stress concentration around initially present flaws, are process-controlled^[3]. These factors translate into strain and stress fields inside the material, which govern its likelihood of cracking. Moreover, several studies have correlated food materials' failure during drying with high moisture content gradients^[4,5]. This, in turn, implies high strain and stress gradients.

Over the last decades, modeling the strain and stress inside food materials during drying has attracted great interest, and several models have been developed. Some models were empirical, others were based on linear or non-linear correlations, and a third group was mechanistic. Readers are referred to the excellent reviews of Defraeye^[6], Katekawa and Silva^[7], Mahiuddin et al.^[8], Mayor and Sereno^[9], Purlis et al.^[10], and Rahman et al.^[11] for a detailed

presentation of these models. For the convective drying of bananas, linear empirical models^[12,13], non-linear empirical models^[14,15], and mechanistic models^[2,16–19] have been used. However, empirical models are merely data-fitting and provide no insight into the underlying transport mechanisms. They can only yield average strain and not spatiotemporal strain distribution. They cannot predict average stress or stress distribution. Additionally, their validity is limited within the boundaries of the experimental conditions, and results cannot be generalized to other processing conditions^[9,10]. Likewise, mechanistic models of banana drying did not couple transport and deformation. For example, Seyedabadi et al.^[18] used the Arbitrary Lagrangian–Eulerian method (ALE) in modeling banana drying but formulated the transport equations in the Eulerian frame. Some mechanistic models of banana drying employed simplifying assumptions about the transport mechanism, assuming, for instance, that the fluid transport was Fickian throughout the drying^[2,16,18,20,21]. Some banana layers approach the glass transition temperature during drying, requiring non-Fickian transport modeling. The equation developed by Caballero-Cerón et al.^[22] predicts glass transition temperatures ranging from 53.6 °C for anhydrous bananas to 25 °C for samples having 0.035 g/g solids moisture content. Therefore, the moisture content of the external layers of bananas is expected to approach the glass transition band for moisture transport to become non-Fickian.

Thus, this research aims to develop a multiscale model of strain and stress during banana drying. To achieve this, this work uses Hybrid Mixture Theory-based equations coupling the strain and stress development with the mechanisms of transport of mass and heat. The derivation process captured microscale phenomena such as viscoelastic relaxation. Hence, the equations account for the non-Fickian fluid transport behavior in the glass transition vicinity. Additionally, the mass and heat transport equations are formulated in the Lagrangian frame, thus incorporating the effect of the matrix deformation on the transport.

2. Model development

2.1. System description

Figure 1 provides the geometry and a three-scale schematization of the banana (*Musa paradisiaca*). Bananas used in the model and experimental validation studies were disc-shaped slices. The 3D slice was reduced to a 2D rectangle in an axisymmetric coordinate system under symmetry. The left and bottom edges formed the axis of symmetry and plane of symmetry, respectively, and the other two constituted the external boundaries where heat and mass exchange with the ambient air occurred. The banana pulp was assumed to be a three-scale, two-phase system consisting of solid and water phases. At the microscale (of the order of microns), the solid (predominantly biopolymers: amylose, amylopectin, pectin, and hemicellulosic

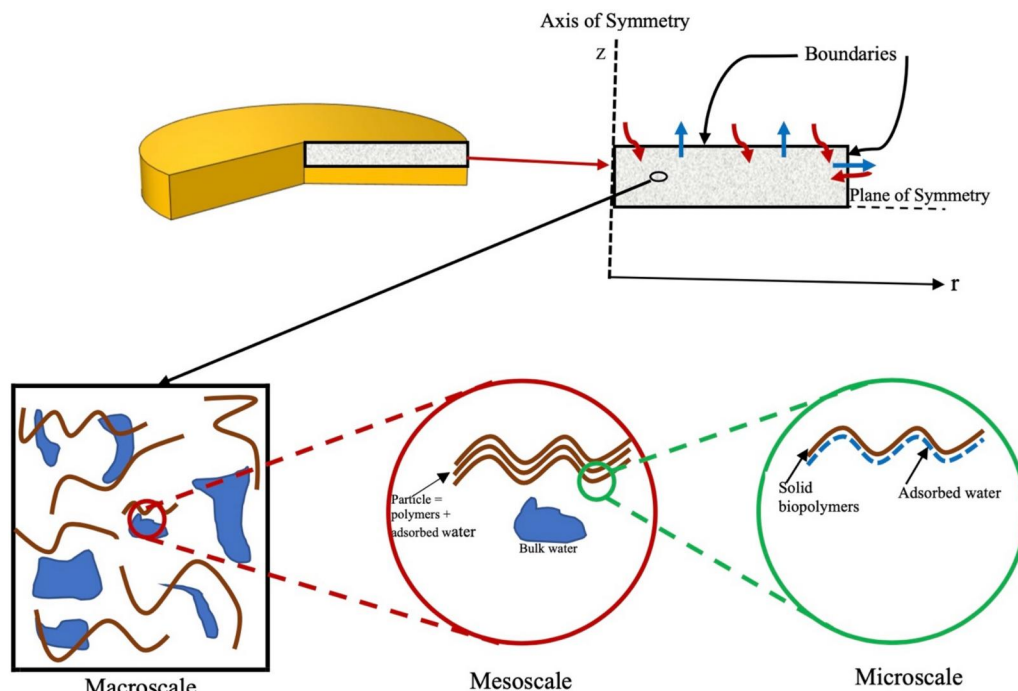


Figure 1. Geometry and three-scale structure of the banana.

polysaccharides) and the vicinal water were distinct. Polymer relaxation phenomena took place at this scale. At the mesoscale (of the order of millimeters), the biopolymer and the vicinal water merged and were no longer distinguishable. However, the banana was still a two-phase system. At this scale, the solid phase was composed of the particle (biopolymer and adsorbed water), and the fluid phase was made up of bulk water. The solid particles and bulk water were homogenized at the macroscale, forming a homogeneous mixture at each spatial point. In this study, a two-scale model was used in which the distinction between micro and mesoscales was not made^[23].

2.2. Model assumptions

In developing the mass and energy transfer equations during banana drying, the following assumptions were made:

1. Inside the macroscale representative elementary volume (REV), the banana slice was treated as a homogeneous, isotropic, linear viscoelastic body consisting of solid viscoelastic and viscous water phases.
2. The fluid transport was assumed to be saturated due to the high initial moisture content. Therefore, the volume change was assumed to compensate for the moisture loss during drying. In food materials, this ideal shrinkage behavior is expected at low drying rates, allowing the material to remain in a rubbery state for most of the drying process until it reaches a moisture content lower than the glass transition moisture content.
3. The polymeric solid and the water phases were assumed incompressible at the microscale, although shrinkage of the matrix was still allowed at the macroscale.
4. The polymeric solid and the water phases were assumed to be at local thermal equilibrium within the REV. However, a large-scale temperature variation between two spatial points was still allowed.
5. The strain in banana slices was assumed to result from the moisture loss. Strain due to thermal expansion was not considered, as it is expected to be significantly smaller than the moisture loss-based strain.
6. The material points were assumed not to rotate during volume change. The volume change occurred in the r- and z-directions. The banana slices remained cylindrically symmetric throughout the drying. This implies that, although the

banana slices experienced shrinkage in the r and z directions, they preserved their original shape and symmetry around the axis passing through the center.

7. The banana slices were assumed to be strain and stress-free, and the moisture was considered to be uniformly distributed at the onset of the drying.

2.3. Generalized two-scale transport equation in Eulerian coordinates

The generalized two-scale transport equation of Takhar^[24] was used to model the movement of water inside the banana slice. In Eulerian coordinates, this equation is:

$$\frac{D^s(\varepsilon^w \rho^w)}{Dt} + \nabla_E \cdot (\varepsilon^w \rho^w v_E^{w,s}) - \varepsilon^w \rho^w \frac{\dot{\varepsilon}^s}{\varepsilon^s} = 0 \quad (1)$$

In (1), D^s/Dt and dot over a variable ($\dot{\varepsilon}^s$) represent the material time derivative taken by following the motion of a material point fixed on the solid particle, ε^w and ε^s are the volume fractions of the water and solid phases, respectively. ρ^w is the water phase density and ∇_E is the spatial gradient in Eulerian coordinates. $v_E^{w,s}$ represents the velocity of the water phase relative to the solid phase and is equal to:

$$v_E^{w,s} = v_E^w - v_E^s \quad (2)$$

At the microscale, water was assumed to be incompressible. Thus, we have:

$$\frac{D^s \rho^w}{Dt} = 0 \quad (3)$$

In addition, for a saturated system, the volume fractions are constrained by:

$$\varepsilon^s + \varepsilon^w = 1 \quad (4)$$

Using (3) and (4) to simplify (1) resulted in:

$$\rho^w \frac{D^s(\varepsilon^w)}{Dt} + \nabla_E \cdot (\varepsilon^w \rho^w v_E^{w,s}) + \varepsilon^w \rho^w \frac{\dot{\varepsilon}^w}{(1 - \varepsilon^w)} = 0 \quad (5)$$

2.4. Multiscale energy balance equation

The transfer of heat inside the banana was modeled using the multiscale heat transfer equation of De Vries^[25]. In Eulerian coordinates and for a saturated system, this equation can be expressed as:

$$\sum_{\alpha=s,w} \varepsilon^\alpha \rho^\alpha C_p^\alpha \frac{D^\alpha T}{Dt} - \nabla_E \cdot \left(\sum_{\alpha=s,w} (\varepsilon^\alpha k^\alpha) \nabla_E T \right) = 0 \quad (6)$$

where ε^α represents the volume fraction of the α -phase (water and solid), C_p^α and k^α are the specific heat and the thermal conductivity of the α -phase, and $\frac{D^\alpha T}{Dt}$ is the material time derivative of the temperature calculated by fixing the material point to the α -phase (water and solid).

In (6), the second term on the left-hand side (LHS) accounts for the heat transferred by conduction. The first term of the LHS combines heat transferred by convection by the moving water and thermal energy buildup as a temperature change in the material. Equation (6) was developed to represent these last two components explicitly by converting the material time derivative from the water phase to the solid phase.

The following relation was used to relate the temperature material time derivative with respect to the water phase to the material time derivative with respect to the solid phase^[26]:

$$\frac{D^w T}{Dt} = \frac{D^s T}{Dt} + v_E^{w,s} \cdot \nabla_E T \quad (7)$$

In addition, the material time derivative of the temperature following the velocity of a particle in the solid phase was related to the time and spatial derivatives of temperature by the following equation:

$$\frac{D^s T}{Dt} = \frac{\partial T}{\partial t} + v_E^s \cdot \nabla_E T \quad (8)$$

Combining (7) and (8), and using the result in (6) yielded the following expression for the energy balance equation in Eulerian coordinates:

$$\begin{aligned} & \sum_{\alpha=s,w} \varepsilon^\alpha \rho^\alpha C_p^\alpha \left[\frac{\partial T}{\partial t} + (v_E^s + v_E^{w,s}) \cdot \nabla_E T \right] \\ & - \nabla_E \cdot \left(\sum_{\alpha=s,w} (\varepsilon^\alpha k^\alpha) \nabla_E T \right) \\ & = 0 \end{aligned} \quad (9)$$

The velocity of the solid v_E^s in (9) is nonzero since the solid structure shrinks during drying. It was calculated using the mass balance equation for the solid phase^[26]:

$$\frac{D^s \varepsilon^s}{Dt} + \varepsilon^s \nabla_E \cdot v_E^s = 0 \quad (10)$$

The velocity of the water phase with respect to the solid phase $v_E^{w,s}$ in (5) and (10) was calculated using the generalized Fick's law detailed in the next section.

2.5. Generalized Fick's law in Eulerian coordinates

The velocity of the water phase with respect to the solid phase was calculated using the generalized Fick's

law of Takhar^[24]. In Eulerian coordinates and for a saturated system, the equation can be expressed as:

$$v_E^{w,s} = -\varepsilon^w (D^w \nabla_E \varepsilon^w + B_c \nabla_E \sigma) \quad (11)$$

where D^w represents the water diffusivity coefficient, B_c is a material coefficient relating the viscoelastic relaxation to the fluid flow, and σ represents the viscoelastic stress.

The first and second terms on the RHS represent the contributions of the concentration gradient and stress in polymers, respectively, to the flow of water.

The generalized Maxwell model is used to represent the viscoelastic stress inside the material. The mechanical analog of this model is formed by a spring coupled in parallel with m Maxwell elements. Each Maxwell element is composed of a spring and a dash-pot in series. The corresponding stress relaxation function $G(t)$ can be measured by uniaxial or shear testing and described by the following Prony series:

$$G(t) = G_0 + \sum_{m=1}^p G_m e^{-t/\lambda'_m} \quad (12)$$

where G_0 is the stress at infinite relaxation time, and G_m and λ'_m are the stress coefficient and the rescaled relaxation time of the m th Maxwell element, respectively.

The rescaled relaxation times λ'_m relate to the relaxation times λ_m by the following equation:

$$\lambda'_m = \frac{\lambda_m}{a_M a_T} \quad (13)$$

where a_M and a_T are the moisture and temperature shift factors.

Thus, the viscoelastic stress σ is:

$$\sigma(t) = \sum_{m=0}^p \int_0^t G_m \exp\left(-\frac{t-\tau}{\lambda'_m}\right) \frac{\partial E_{MM}^s}{\partial \tau} d\tau \quad (14)$$

Here E_{MM}^s is the first invariant of the strain tensor and relates to the water volume fraction by^[27]:

$$E_{MM}^s = \frac{\varepsilon^w - \varepsilon_0^w}{1 - \varepsilon^w} \quad (15)$$

Equation (14) links the strain induced by the water loss to the viscoelastic stress generated inside the material. As moisture exits the material, the solid structure shrinks to compensate for the moisture loss, and the shrinkage creates stress. Then, the polymers release that stress by relaxing in a time-dependent manner.

The stress equation as given by (14), involves a time-dependent integral. This equation cannot be solved directly when using finite element-based commercial software like COMSOL Multiphysics version

5.6 (Burlington, MA, USA). However, since each m th term in the stress equation forms a convolution, the integral in (14) can be transformed into a series of $P + 1$ ordinary differential equations (ODEs) by applying the Laplace transformation, as described by Takhar^[3]. By performing the Laplace transformation of both sides of an m th term in (14), rearranging, and using the inverse Laplace transformation, the following series of ODEs is obtained:

$$\frac{\partial Z_m}{\partial t} + \frac{1}{\lambda_m} Z_m = G_m \frac{\partial E_{MM}}{\partial t}, \quad m = 0 \text{ to } p \quad (16)$$

In (16), Z_m ($m = 0$ to p) represents the viscoelastic stress of the m th Maxwell element. The contribution of the spring (G_0) to the total viscoelastic stress is recovered by taking a large (approaching infinity) relaxation time ($\lambda_0 \rightarrow \infty$). Therefore, the total viscoelastic stress can be calculated using the following equation:

$$\sigma(t) = \sum_{m=0}^p Z_m \quad (17)$$

2.6. Transforming from Eulerian to Lagrangian coordinates

During drying, food materials shrink, and the computational domain changes with time for a coordinate system fixed in space *a priori*, as with Eulerian coordinates. Hence, the solution of the transport equations with the finite element method would be complicated since the spatial location of the material points changes with time, and a moving mesh needs to be used. The Eulerian and Lagrangian operators for the cylindrical coordinate system are related, and the relation was used to convert transport equations from Eulerian to Lagrangian coordinates. Lagrangian coordinates are attached to the material, and as the material shrinks, the coordinates shrink accordingly.

The banana slices used in the model were cylindrical, and the reference state used was the initial state. A well-defined relation in continuum mechanics between the differential volumes in the deformed (dv) and the undeformed (dV) configurations of materials is^[28]:

$$dv = j dV \quad (18)$$

where j is the determinant of the Jacobian matrix. Banana slices used in the model and the experiments had a cylindrical shape. Thus, (18) becomes:

$$r dr d\theta dz = j R dR d\phi dZ \quad (19)$$

During drying, banana slices were assumed to remain geometrically similar ($r = \zeta R$, $z = \zeta Z$, $d r = \zeta dR$, $d z = \zeta dZ$ or $\partial R / \partial r = \partial Z / \partial z = 1 / \zeta$) and the

material points were assumed not to rotate in the angular direction ($d\theta = d\phi$)^[29]. With these assumptions, (19) can be written as:

$$j = \zeta^3 \quad (20)$$

In axisymmetric cylindrical coordinates, the Eulerian gradient operator can be represented by:

$$\nabla_E = \frac{\partial}{\partial r} \hat{e}_r + \frac{\partial}{\partial z} \hat{e}_z \quad (21)$$

Applying the chain rule to (21) and incorporating (20) yields the relation between the Eulerian and Lagrangian operators.

$$\begin{aligned} \nabla_E &= \frac{\partial}{\partial r} \hat{e}_r + \frac{\partial}{\partial z} \hat{e}_z = \frac{\partial R}{\partial r} \frac{\partial}{\partial R} \hat{e}_R + \frac{\partial Z}{\partial z} \frac{\partial}{\partial Z} \hat{e}_Z \\ &= \frac{\partial R}{\partial r} \left(\frac{\partial}{\partial R} \hat{e}_R + \frac{\partial}{\partial Z} \hat{e}_Z \right) = \frac{1}{\zeta} \nabla_L = j^{-1/3} \nabla_L \end{aligned} \quad (22)$$

The determinant j of the Jacobian matrix can be expressed in terms of volume fractions.

At the microscale, the following relation holds for the solid phase:

$$\varepsilon^s \rho^s j^s = \varepsilon_0^s \rho_0^s \quad (23)$$

Assuming that the solid phase is incompressible at the microscale ($\rho^s = \rho_0^s$), (23) yields:

$$j^s = \frac{\varepsilon_0^s}{\varepsilon^s} = \frac{1 - \varepsilon_0^w}{1 - \varepsilon^w} \quad (24)$$

Finally, (22) can be expressed as:

$$\nabla_E = j^{-1/3} \nabla_L = \left(\frac{1 - \varepsilon_0^w}{1 - \varepsilon^w} \right)^{-1/3} \nabla_L \quad (25)$$

In Lagrangian coordinates, as the time derivative follows the solid material particle, D^s/Dt was replaced by $\partial/\partial t$.

2.7. Material properties

In the derivation of HMT-based models, the field equations (mass, momentum, energy, and entropy balance laws) are set at the microscale in a form similar to single-scale balance equations. The balance laws are then upscaled to higher scales to yield their multiscale counterparts^[30]. The constitutive theory, where the specific nature of the materials is included, is formulated at the macroscale, the scale at which most food materials' properties are measured. Thus, the literature's thermophysical, rheological, and transport properties can be readily utilized to solve HMT-derived transport equations.

The banana's thermophysical, transport, and rheological properties used to solve the transport and stress equations are listed in Tables 1 and 2. The solid-phase densities (ρ^s), specific heat (C_p^s), and thermal conductivity (k^s) were determined using correlations of Bart-Plange et al.^[32]. The authors measured properties between 0.185 and 0.50 g/g total moisture content range. Properties of the solid phase were calculated assuming a 0 g/g total moisture content. The moisture diffusivity (D^w) equation used in this study was from work by Bains and Langrish^[17]. The authors dried bananas between 40 °C and 80 °C and assumed an Arrhenius-type dependency of the diffusion coefficient to the temperature.

The moisture equilibrium relation by Ajibola^[35] was used to calculate the water activity (a_w) at the surface of bananas as a function of the moisture content and temperature. The equation is a modified Halsey model fitted to the desorption data of bananas dried between 40 °C and 70 °C.

The viscoelastic coefficient B_c (Table 2) was evaluated during fluid transport simulations by the inverse

method described by Singh et al.^[36]. The coefficient was determined by a two-step process. In the first step, the optimum B_c at a given temperature was selected as the value yielding the lowest root-mean-square error (RMSE) when predicted and experimental average moisture content values were compared. Measurements and predictions were compared at 40, 60, and 80 °C, and it was found that optimum values obtained following the above procedure differed markedly. In the second step, an overall temperature-dependent expression for the B_c coefficient was obtained by nonlinear regression. The form of the equation was suggested by plotting the optimum B_c values versus temperature and physical arguments. The B_c coefficient transforms the viscoelastic stress gradient into a velocity term component. The sign of the B_c determines whether the contribution of the viscoelastic relaxation to transport will be positive or negative. Therefore, a temperature-dependent B_c was not expected to flip its sign during computation as the temperature increased. Using the above physical argument, a temperature-dependent expression for B_c

Table 1. Physical and thermophysical properties of the banana used in the model.

Properties	Relation/value	References
Initial diameter d_i (m)	31×10^{-3}	Measured
Initial thickness th_i (m)	7×10^{-3}	Measured
Density* (kg/m ³)		
Water density (ρ^w)	$838.466135 + 1.400506T - 3.0112376 \times 10^{-3}T^2 + 3.718223137 \times 10^{-7}T^3$	[31]
Solid density (ρ^s)	1649	[32]
Specific heat* (J kg ⁻¹ K ⁻¹)		
Water (C_p^w)	$12010.147 - 80.407T + 0.310T^2 - 5.382 \times 10^{-4}T^3 + 3.625 \times 10^{-7}T^4$	[33]
Solid (C_p^s)	1742.3	[32]
Thermal conductivity* (W m ⁻¹ K ⁻¹)		
Water (k^w)	$0.869 + 8.949 \times 10^{-3}T - 1.584 \times 10^{-5}T^2 + 7.975 \times 10^{-9}T^3$	[34]
Solid (k^s)	0.1206	[32]

*T in Celsius.

Table 2. Transport and rheological properties of the banana used in the model.

Properties	Relation/value	References
Transport properties*		
Water diffusivity* (D^w) m ² /s	$1.36 \times 10^{-7} \exp(-1610/T)$	[17]
Viscoelastic coefficient (B_c) m ³ /kg	$7.60075 \times 10^{-25} \exp(T/13.6073)$	
Water activity (a_w)	$\exp[-\exp(9.83 - 2.019 \times 10^{-2}T)M^{-1.321}]$	[35]
Viscoelastic properties** Abedi and Takhar ^[37]		
Stress coefficients, G_m (MPa) (see 13)	$G_0 = 0.00261 \left[\frac{(T + 273)}{T_0} \right] \left(\frac{M}{M_0} \right)$ $G_1 = 0.01319 \left[\frac{(T + 273)}{T_0} \right] \left(\frac{M}{M_0} \right)$ $G_2 = 0.010 \left[\frac{(T + 273)}{T_0} \right] \left(\frac{M}{M_0} \right)$	
Relaxation times (see 13)	$\lambda'_1 = 176.7 / (a_T a_M)$ $\lambda'_2 = 43.8 / (a_T a_M)$	
a_M	$\exp(5.14672 - 3.19165M)$	
a_T	$\exp(5.01412 - 0.06106T)$	

*T is in K.

** $T_0 = 353.15$ K, $M_0 = 1.53$ g/g solids, T is in °C, M is in g/g solids.

Table 3. Physical and mechanical properties of the drying air.

Properties	Relation/value	References
Molecular weight (M_2) kg/mol		
Water (M_w)	18.01528×10^{-3}	
Dry air (M_a)	28.96546×10^{-3}	
Pressure (P) Pa		
Saturated vapor (P_{sat})	$\text{Exp} \left[\frac{-6096.9385 \times T^{-1} + 21.2409642 - 0.02711193 \times T}{+ 0.1673952 \times 10^{-4} T^2 + 2.43502 \ln T} \right]$	[42]
Vapor (P^v)	At the surface $P_{\text{surf}}^v = P_{\text{sat}} \times a_w$, P_{sat} evaluated at $T = T_f$ At the ambient air $P_{\text{amb}}^v = P_{\text{sat}} \times RH$, P_{sat} evaluated at $T = T_{\text{amb}}$	
Atmospheric (P_{atm})	101,325	
Density (ρ^g) m ³ /kg		
Gas (mixture of dry air and vapor) ρ^g	$\frac{P_{\text{atm}} - 0.378 \times \frac{P^v}{P_{\text{amb}}}}{287.1 \times T}$	[42]
Dry air (ρ^a)	$\rho^a = \frac{M_w \times P_{\text{atm}}}{R_a T}$	Ideal gas
Water vapor (ρ^v)	At the surface: $\rho_{\text{surf}}^v = \frac{M_w \times P_{\text{surf}}^v}{R_a M_w \times P_{\text{amb}}^v}$ At the ambient air: $\rho_{\text{amb}}^v = \frac{P^v}{R_a T}$	Ideal gas
Dynamic viscosity (μ^g) Pa.s		
Dry air (μ^a)	$-8.383 \times 10^{-7} + 8.357 \times 10^{-8} T - 7.694 \times 10^{-11} T^2 + 4.644 \times 10^{-14} T^3 - 1.06585607 \times 10^{-17} T^4$	[31]
Water vapor (μ^v)	$1.420 \times 10^{-6} + 3.835 \times 10^{-8} T - 3.852 \times 10^{-12} T^2 + 2.102 \times 10^{-15} T^3$	[31]
Gas (mixture of dry air and vapor) μ^g	$\mu^g = \frac{y^a \mu^a}{y^a + y^v \phi^{av}} + \frac{y^v \mu^v}{y^v + y^a \phi^{va}}$	[34]
	$\phi^{av} = \frac{[1 + (\mu^a / \mu^v)^{1/2} (M_w / M_a)^{1/4}]^2}{\{8[1 + (M_a / M_w)]\}^{1/2}}$; $\phi^{va} = \phi^{av} \frac{\mu^a M_a}{\mu^v M_w}$; $y^a = 1 - y^v$ and $y^v = \frac{P^v}{P^g}$	
Specific heat (C_p^g) J kg ⁻¹ K ⁻¹		
Dry air (C_p^a)	$1047.637 - 0.373 T + 9.453 \times 10^{-4} T^2 - 6.024 \times 10^{-7} T^3 + 1.286 \times 10^{-10} T^4$	[31]
Water vapor (C_p^v)	$13604.734 - 90.430 T + 0.277 T^2 - 4.213 \times 10^{-4} T^3 + 3.184 \times 10^{-7} T^4 - 9.561 \times 10^{-11} T^5$	[31]
Gas (mixture of dry air and vapor) C_p^g	$C_p^g = x^a C_p^a + x^v C_p^v$ with $x^a = 1 - x^v$ and $x^v = \frac{\rho^v}{\rho^v + \rho^a}$	[43]
Thermal conductivity (k^g) W/(m.K)		
Dry air (k^a)	$-2.276 \times 10^{-3} + 1.155 \times 10^{-4} T - 7.903 \times 10^{-8} T^2 + 4.117 \times 10^{-11} T^3 - 7.439 \times 10^{-15} T^4$	[34]
Water vapor (k^v)	$1.317 \times 10^{-4} + 5.150 \times 10^{-5} T + 3.896 \times 10^{-8} T^2 - 1.368 \times 10^{-11} T^3$	[34]
Gas (mixture of dry air and vapor) k^g	$k^g = \frac{y^a k^a}{y^a + y^v \phi^{av}} + \frac{y^v k^v}{y^v + y^a \phi^{va}}$	[34]
Enthalpy of vaporization of water (ΔH_{vap}) J/kg	$\Delta H_{\text{vap}} = \Delta H_{\text{vap,ref}} \left(\frac{1 - T_r}{1 - T_{r,\text{ref}}} \right)^{0.38}$ $\Delta H_{\text{vap,ref}} = 4.49810 \times 10^7$ J/K _{mol} $T_{\text{ref}} = 273.16$ K; $T_c = 647.096$ K; $T_r = T/T_c$ $T_{r,\text{ref}} = T_{\text{ref}}/T_c = 0.422$	[42]
Universal gas constant (R) J mol ⁻¹ K ⁻¹	8.3145	[42]
Coefficient of diffusion of water vapor in gas (D^v) m ² /s	$-2.775 \times 10^{-6} + 4.479 \times 10^{-8} T + 1.656 \times 10^{-10} T^2$	[44]

that would yield strictly positive values was researched. Therefore, the exponential function (26) was chosen to represent the overall temperature-dependent B_c coefficient.

$$B_c = A \exp((T - 273)/B) \quad (26)$$

where T is in K.

The coefficients A and B were determined by non-linear regression to equal $A = 7.60075 \times 10^{-25}$, and $B = 13.6073$ with an RMSE of 0.503212×10^{-13} or a normalized NRMSE of 22.7%.

In the literature, constant B_c values were used^[3,27,36]. However, in this work, the optimum B_c value varies with the temperature, with high temperatures requiring higher B_c values. This finding can be explained using the free volume theory. The total volume occupied by polymers comprises Van der Walls

and free volumes. The free or unoccupied volume allows polymers to accommodate mechanical changes occurring at the macroscopic level, giving rise to the viscoelastic response^[37]. Small penetrant molecules like water diffuse also through the free volume. In polymer physics literature, several measurements using positron annihilation spectroscopy (PALS) have shown that both the van der Waals and the free volume increase with the temperature, but above the glass transition, the free volume increases at a rate dramatically higher than the van der Waals volume^[38,39]. Therefore, polymer mobility increases significantly and the time scale of polymer relaxation changes. Thus, the increase in the B_c coefficient at high temperatures indicated the greater influence polymer relaxation had on the flow as the temperature was raised.

Table 4. Equations/values for calculating the initial (IC) and boundary conditions (BC).

Properties	Relation/value	References
Mass transfer coefficient (h_m)	$h_m = Sh D^v/L$ [m/s] $L = d_i = 31 \times 10^{-3}$ [m]	[42]
Sherwood number (Sh)	$Sh = 0.0296Re^{4/5}Sc^{1/3}$	[45]
Schmidt number (Sc)	$Sc = \mu^a/\rho^a D^v$	[42]
Reynolds number (Re)	$Re = L v^a \rho^a/\mu_a$	[42]
Heat transfer coefficient (h_T)	$h_T = Nu k^v/L$ [W/(m ² ·K)] $L = d_i = 31 \times 10^{-3}$ [m]	[42]
Nusselt number (Nu)	$Nu = 0.0296Re^{4/5}Pr^{1/3}$	[45]
Prandtl number (Pr)	$Pr = \mu^a C_p^a/k^a$	[42]
Stress equation (14 and 17)	IC: $\sigma = 0$, Hence $Z_m = 0$ for $m = 0$ to p	
Water mass balance (26)	IC: $\varepsilon^w = \varepsilon_i^w$ BC: at $r = d_i/2$ or $z = th_i/2$; water flux: $Q_w = h_m(\rho_{amb}^v - \rho_{surf}^v)$ [kg/(m ² ·s)]	
Solid mass balance (27)	IC: $v^s = v_i^s = 0$ m/s BC: at $r = 0$ or $z = 0$; $v^s = 0$ [m/s]	
Energy balance (28)	IC: $T = T_i = 298.15$ K BC: at $r = d_i/2$ or $z = th_i/2$; heat influx [W/m ²]: $-K\nabla T \cdot n _{surf} = h_T(T_{amb} - T_{surf}) - h_m(\rho_{surf}^v - \rho_{amb}^v)\Delta H_v$	

The coefficients G_0 and G_m in the viscoelastic stress equation (14) and the relaxation times λ_m (13) were obtained from the work of Abedi and Takhar^[40]. The authors reported the coefficients of the two-element generalized Maxwell model (G_0 , G_1 , and G_2) and the relaxation times (λ_1 and λ_2) of bananas as a function of drying temperature (40–80 °C) and moisture contents (0.17–1.84 g/g solids). A master curve was constructed from these data following the procedure described by Hammerle and Mohsenin^[41].

The moisture content (M) was calculated from the volume fraction of water (ε^w) and vice versa using:

$$M = \frac{\varepsilon^w \rho^w}{\rho^s(1 - \varepsilon^w)} \quad (27)$$

The average moisture content (\bar{M}) over the entire domain was calculated by integrating moisture content at different spatial locations:

$$\bar{M} = \frac{\int M dV}{\int dV} \quad (28)$$

2.8. Initial and boundary conditions

2.8.1. Initial conditions

The properties of the drying air are detailed in Table 3 and the initial conditions for the transport and stress equations are listed in Table 4. At the onset of the drying, the moisture content and temperature in bananas were assumed to be uniformly distributed. The initial moisture contents (M_0) varied between 1.69 and 1.98 g/g solids. The initial temperature (T_i) was set to room temperature (25 °C). To solve the viscoelastic stress equation (14), bananas were assumed to be stress-free at the beginning of drying.

Table 5. Hedonic scale for crack evaluation.

Crack index	Number of cracks	Maximum limits of	
		Crack length (L)	Crack depth (D)
0	0	0	0
1	1–4	$L < \frac{1}{2} R$	$D < 1$ mm
2	5–8	$\frac{1}{2} R < L < R$	1 mm $< D < 3$ mm
3	9–12	$R < L < \frac{3}{2} R$	3 mm $< D < 5$ mm
4	>13	$L > \frac{3}{2} R$	$D > 5$ mm

R: Sample radius, L: Crack length, D: Crack depth.
When multiple cracks are present, the crack length (L) and depth (D) refer to those of the largest crack.

2.8.2. Heat and Mass transfer coefficients

The water and energy balance equations (5 and 9) were solved by applying the flux boundary conditions provided in Table 4 at the surface of the banana slice. These boundary conditions account for the transfer of heat and mass during the drying process. For the heat flux boundary condition, energy input due to convective heating from hot ambient air to the material and loss due to water evaporation in the surface boundary film were included (Table 4).

The critical parameters for the boundary fluxes calculation are the mass (h_m) and heat (h_T) transfer coefficients (Table 4). h_m was calculated using the Sherwood–Reynolds–Schmidt correlation for the average convective mass transfer for forced convection over a flat plate, and h_T was computed using the Nusselt–Reynolds–Prandtl correlation for the local convective heat transfer for the same type of flow and geometry.

2.8.3. Properties of the drying gas

During drying, a boundary layer forms as a thin film over the surface, playing a critical role in heat and mass transfer. Thus, the properties of the drying gas, a mixture of dry air and water vapor, were evaluated at the film temperature (T_f), defined as the average of the surface temperature of the banana slice and the

ambient air temperature.

$$T_f = \frac{T + T_{amb}}{2} \quad (29)$$

Here, T and T_{amb} represent the banana slice's surface and ambient air temperature, respectively.

3. Materials and methods

3.1. Experimental procedures

3.1.1. Drying experiments

Experiments were conducted to validate the model predictions of the average moisture content, temperature, and volumetric strain. Bananas (*Musa paradisiaca*) that were used in the validation studies were purchased from a local grocery store and screened by refractometry to form groups of a uniform degree of maturity. The fruits with sugar levels between 25% and 31% Brix were selected for experiments. Compared to the 7 trade visual indices mentioned by Mendoza et al.^[46], they corresponded to the ripening indices 5 and 6. The fruits were manually peeled and sliced using a knife and a round cookie cutter, resulting in small disks with a diameter of 31 mm and a thickness of 7 mm.

The drying experiments were conducted in an environmental chamber (Associated Environmental Systems, Ayer, MA), providing an airflow of 5.15 m/s perpendicular to the pans and allowing control over the temperature and relative humidity. Various temperature and RH combinations were used between 40–80 °C and 10–20%, respectively. Each drying run for the validation studies lasted four hours.

3.1.2. Moisture content measurement

Initial moisture content values were measured by the air oven method, AACC 44-15.02^[47], with slight modification. AACC 44-15.02 recommends a two-stage drying process for samples with a moisture content exceeding 13%. The prescribed protocol involves an initial stage of oven drying for a duration of 14–16 h, followed by grinding and a subsequent one-hour oven drying stage. However, in this study, moisture measurements were conducted using a single-stage process, which was extended over a prolonged duration. Preliminary observations indicated that the weight of oven-dried banana slices did not change after 24 h of drying at 105 °C. Consequently, it was determined that drying banana slices for a period of 24 h would result in a fully dried state. Therefore, for each fruit, six replicates were dried in an air oven at 105 °C for 24 h, and the initial moisture content on a

dry basis was the average of the replicate's values. For subsequent moisture content values at a given drying time t , samples were weighted before the experiment and after withdrawal from the chamber. Moisture contents were then obtained from the information on the initial value and the weight loss. Six replicates were collected at each data collection point.

3.1.3. Temperature measurement

The evolution of temperature during drying was measured at three different positions using thermocouples coupled to a 4-channel data logger. In brief, two thermocouples were inserted axially into the banana slice: the first at the center, and the second at 0.5 mm from the edge. A third temperature probe was placed directly above the sample to record the ambient air temperature. Data were recorded every 10 s throughout the entire drying duration. For a given drying condition, four replicates were taken, and the average was subsequently calculated.

3.1.4. Volumetric strain measurement

The volumetric strain was determined by measuring the volume change before and after drying using the glass beads displacement method. Five replicates were employed for each data collection point, and samples were collected at 30-min intervals. The volumetric strain was calculated as the average of the replicate values using the formula:

$$S_v = \frac{v - V}{V} \quad (30)$$

where V and v are the initial volume and the volume at a drying time t , respectively.

3.1.5. Crack evaluation

Following validation, additional experiments were conducted to assess whether the drying conditions, designed to reduce stress gradients in the bananas, would result in reduced stress-cracking during experimental trials. These experiments were designed for continuous drying and the fan on/off strategy. In the continuous drying experiments, banana slices were dried at temperatures of 40 °C, 60 °C, and 80 °C and relative humidity levels of 20%, 20%, and 10%, respectively, for varying drying times.

Sets of thirty banana slices were dried continuously on trays, and at specified intervals, the trays were removed from the drying chamber for crack evaluation. A hedonic scale was employed to assess cracks of individual banana slices, using criteria outlined in Table 5, which includes factors such as the number, length, and depth of cracks. Each criterion was rated on a 5-point





	Number of cracks	Crack length (L)	Crack depth (D)	Crack index
	0 ●	0 ●	0 ●	0
	1-4	$L < \frac{1}{2}R$	$D < 1 \text{ mm}$	
	5-8	$\frac{1}{2}R < L < R$	$1 \text{ mm} < D < 3 \text{ mm}$	
	9-12	$R < L < \frac{3}{2}R$	$3 \text{ mm} < D < 5 \text{ mm}$	
	>13	$L > \frac{3}{2}R$	$D > 5 \text{ mm}$	
	0 ●	0 ●	0 ●	2
	1-4	$L < \frac{1}{2}R$	$D < 1 \text{ mm}$	
	5-8	$\frac{1}{2}R < L < R$	$1 \text{ mm} < D < 3 \text{ mm}$	
	9-12	$R < L < \frac{3}{2}R$	$3 \text{ mm} < D < 5 \text{ mm}$	
	>13	$L > \frac{3}{2}R$	$D > 5 \text{ mm}$	
	0 ●	0 ●	0 ●	4
	1-4	$L < \frac{1}{2}R$	$D < 1 \text{ mm}$	
	5-8	$\frac{1}{2}R < L < R$	$1 \text{ mm} < D < 3 \text{ mm}$	
	9-12	$R < L < \frac{3}{2}R$	$3 \text{ mm} < D < 5 \text{ mm}$	
	>13	$L > \frac{3}{2}R$	$D > 5 \text{ mm}$	
	0 ●	0 ●	0 ●	4
	1-4	$L < \frac{1}{2}R$	$D < 1 \text{ mm}$	
	5-8	$\frac{1}{2}R < L < R$	$1 \text{ mm} < D < 3 \text{ mm}$	
	9-12	$R < L < \frac{3}{2}R$	$3 \text{ mm} < D < 5 \text{ mm}$	
	>13	$L > \frac{3}{2}R$	$D > 5 \text{ mm}$	

Figure 2. Use of the hedonic scale for crack evaluation. R: sample radius.

scale, ranging from 0 to 4. The overall crack index for a sample was determined by selecting the highest value among the three evaluation criteria. Examples of the hedonic scale's application can be found in Figure 2. The sum of crack index values for the entire set of thirty banana slices ranged between 0 and 120. The global crack index was then calculated by dividing this sum by 12, rescaling it to a 0–10 scale.

For the fan on/off strategy, banana slices were dried under similar conditions as in continuous drying. At specified intervals, samples were removed from the drying chamber and placed in an oven with the same

temperature. However, in the drying chamber, the fan was on, whereas it was off in the oven. The time spent in the drying chamber corresponded to the fan-on period, while the residence time in the oven was the fan-off period. At 40 °C, periods of 120 min with the fan on (in the drying chamber) alternated with 180 min with the fan off (in the oven) over a 24 h period. At 60 °C, 60 min of the fan on were alternated with 60 min of fan off, and this ratio was reduced to 30 min of the fan on for 60 min of fan off at 80 °C.

For each crack evaluation drying experiment, the first set of banana slices was used to assess the global

crack index, while a second set, subjected to the same conditions, was used for moisture content measurement using the oven method described in point 3.1.2.

3.2. Numerical solution

A commercial finite element software package (COMSOL Multiphysics version 6.1; Comsol, Burlington, MA) was used to implement and solve the transport equations. Given the symmetry displayed by banana slices, a 2D axisymmetric geometry was utilized. Consequently, the disc-shaped slices were transformed into a 2D rectangular domain (see Figure 1) with dimensions of $d_i/2$ length and $th_i/2$ width. The geometry was discretized into 2180 domain elements and 258 boundary elements. A higher element density was implemented toward the boundaries by defining an element ratio of 5, as it was anticipated that temperature changes and water transfer would occur at a higher rate in these regions. Significant shrinkage during banana drying, especially at elevated temperatures, was expected. To track the material's deformation, the arbitrary Lagrangian and Eulerian method (ALE) was employed. A time step of 10 s was specified to capture the effect of the glass transition on moisture transport. The solution was obtained using the MUMPS solver on a Dell desktop, specifically the OptiPlex 5000 model, equipped with a 12th Gen Intel Core i5-12500 processor operating at 3.00 GHz and 16 GB of RAM. The dependent variables calculated included the volume fraction of water ε^w , stress σ , and temperature T .

3.3. Model validation

The model validation involved a comparison with experimental data, specifically focusing on the average moisture content, the center and near-surface temperatures, and the volumetric strain. Mean absolute error (MAE) was chosen as the preferred metric for measuring the model's accuracy. This choice was made because, in the case of RMSE, larger errors carry a higher weight on the RMSE and have the potential to inflate the overall error^[48]. The MAE was calculated using (31) and expressed in the same units as the experimental data.

$$\text{MAE} = \frac{1}{n} \sum_{j=1}^n |y_j - x_j| \quad (31)$$

where n represents the number of experimental data points, y_j and x_j denote the predicted and experimental values, respectively.

4. Results and discussion

4.1. Validation results

The experimental results for the banana's average moisture content, temperature at the center and near the surface, and the volumetric strain were compared with the model predictions.

4.1.1. Moisture profiles

Figure 3(A–C) show the validation data for the multi-scale water balance equation (5). Average moisture content values were collected for drying temperatures of 40 °C, 60 °C, and 80 °C and air relative humidity levels of 20%, 20%, and 10%, respectively. At all drying temperatures, the average moisture content showed a sharp decrease at the beginning of drying, with the rate of decrease becoming more gradual toward the end. At elevated temperatures (60 °C and 80 °C), the drying curves exhibited a quasi-linear shape during the first half of the drying process, and higher drying temperatures resulted in achieving the lowest final moisture content. This rapid initial decrease in the average moisture content of high-moisture foods is a phenomenon observed in the literature and is associated with the constant drying rate period^[49].

The moisture content profiles predicted by the model are in agreement with the experimental values. The MAEs at 40 °C and 20% RH, 60 °C and 20% RH, and 80 °C and 10% RH were 0.022, 0.106, and 0.121 g/g solids, respectively. However, the moisture content prediction at 80 °C and 10% RH was less accurate. The deviation between the model's prediction and the experimental data at 80 °C and 10% RH could be attributed to the uncertainty in the water diffusion coefficient. The diffusion coefficient used in this study was based on the work of Bains and Langrish^[17], for which the banana variety was unspecified. Bananas exhibit significant inter-variety variability in their composition, such as sugars, proteins, or lipids contents^[1], which can impact moisture diffusivity. This variation in moisture diffusivity has been observed in starch-based systems when simple sugars are added to the matrix^[50–52].

4.1.2. Volumetric strain

Figure 4(A–C) display the validation data for the strain equation (15). Predictions at 40 °C were also compared with the shrinkage curve published by Johnson et al.^[13]. Higher drying temperatures led to increased final volumetric strains, with values of

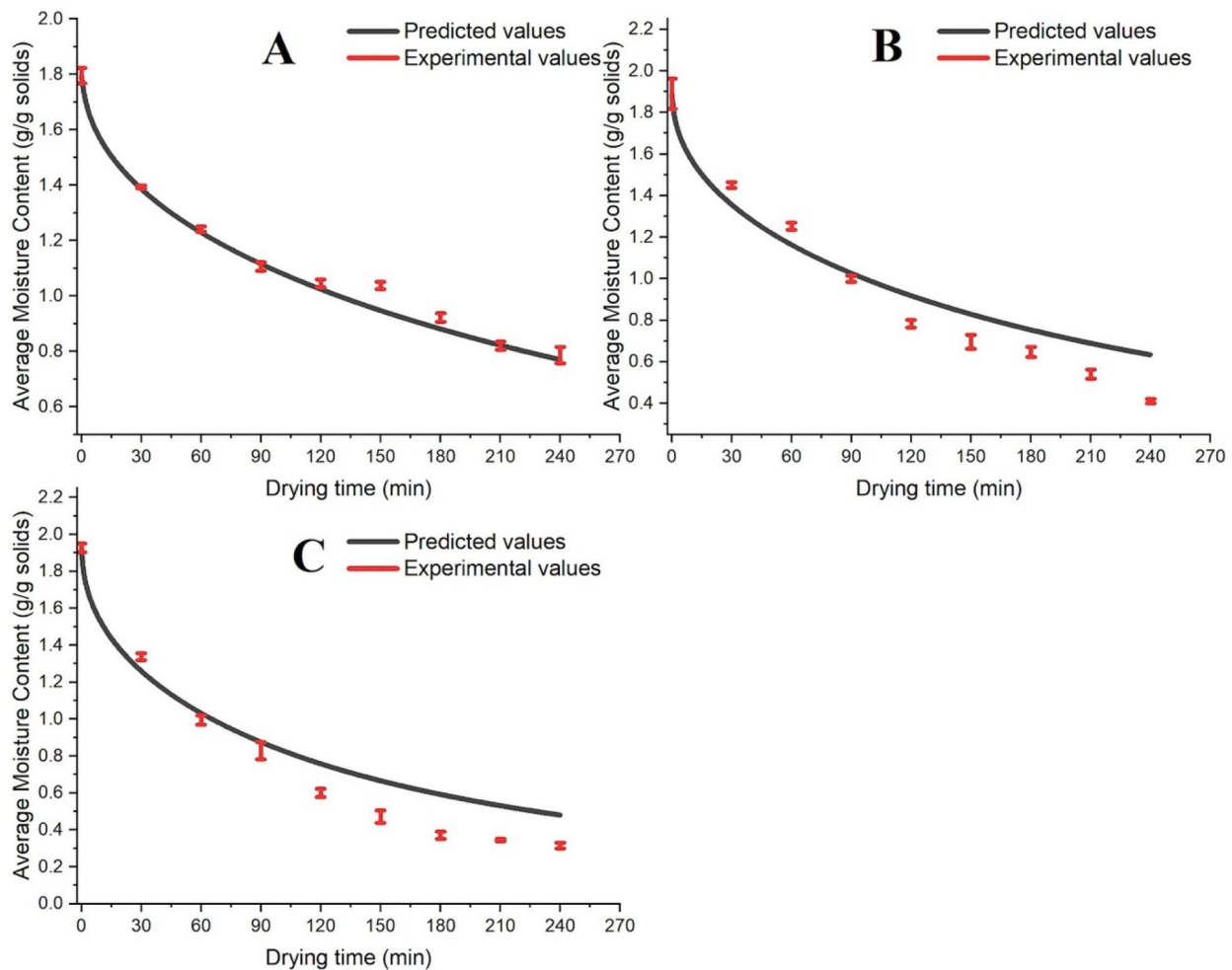


Figure 3. Comparison of predicted and experimental average moisture content values of bananas dried at A) 40°C and 20% RH, B) 60°C and 20% RH, and C) 80°C and 10% RH. Error bars represent standard errors ($n = 6$).

−0.54 at 80°C and 10% RH, −0.52 at 60°C and 20% RH, and −0.44 at 40°C and 20% RH.

The volumetric strain predictions moderately align with the experimental data collected in this study. The most accurate predictions were achieved at 40°C and 20% RH and 80°C and 10% RH, with MAEs of 0.06 and 0.07, respectively. The predictions at 40°C and 20% RH also demonstrated a closer agreement with the data from Johnson et al.^[13]. However, at 60°C and 20% RH, the MAE was 0.13.

Significant differences were observed at all temperatures during the first half of the drying process. However, the prediction and experimental values showed a closer agreement during the second half of drying. The overall error from the model, with MAEs ranging from 0.06 to 0.13, was found to be comparable in magnitude to the uncertainty associated with individual measurements, with the standard error ranging from 0.007 to 0.11. This observation underscores the significant variability in banana behavior regarding shrinkage.

4.1.3. Temperature profiles

The validation data for the multiscale energy balance equation (9) are depicted in Figure 5(A–C). Each figure presents the predicted and experimental temperatures measured at the center of the banana slice, near the surface, and in the ambient air. The experimental curves displayed a consistent profile across all drying temperatures and data collection points. They exhibited a sharp increase at the beginning of drying, followed by an inflection in the subsequent drying stages. The rapid temperature rise marked the heating period, while the inflection points indicated the falling rate period. It is worth noting that the curves did not exhibit a distinct constant rate drying period, except for 80°C, where the center temperature curve flattened after the initial spike and then increased again around 140 min into the drying process. At higher temperatures, both the center and near-surface temperatures increased more rapidly, and the inflection appeared earlier in the drying process compared to lower temperatures. Despite these variations, the center

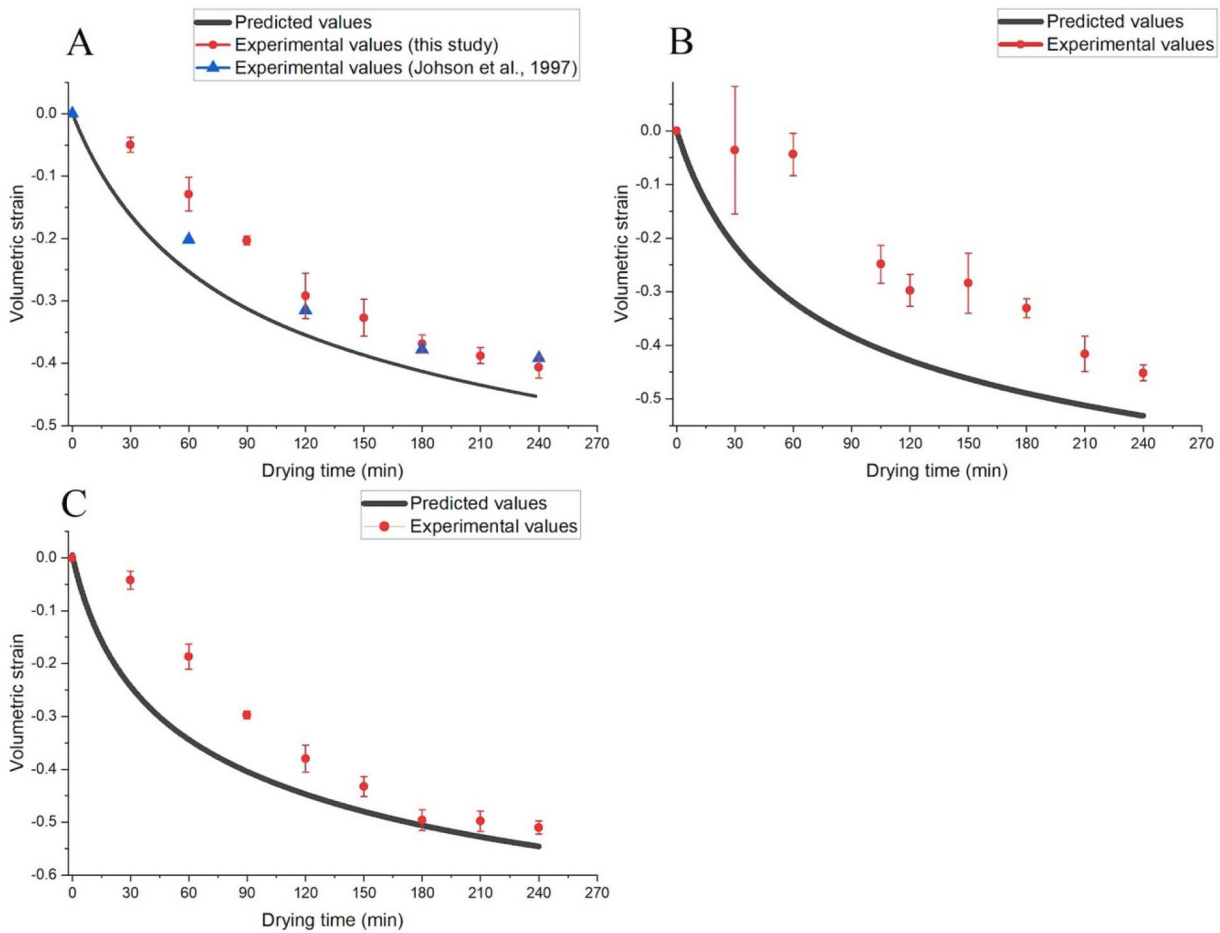


Figure 4. Comparison of predicted and experimental volumetric strain values of bananas dried at A) 40°C and 20% RH, B) 60°C and 20% RH, and C) 80°C and 10% RH. Error bars represent standard errors ($n = 5$).

temperature did not reach the ambient air temperature even after 4 h of drying for all tested conditions.

The MAEs for the center temperature at 40°C, 60°C, and 80°C were 2.1°C, 5.4°C, and 7.7°C, respectively. In contrast, the model predictions for the near-surface temperature were more accurate, with MAEs of 0.6°C, 3.2°C, and 0.9°C at 40°C, 60°C, and 80°C, respectively.

The prediction of the center temperature could be further improved if unsaturated transport (including vapor as a distinct phase) was used. In the current model, the effect of vapor diffusion was lumped into the diffusion coefficient term. Consequently, the heat sink related to water phase changes inside the material was not considered, resulting in model predictions that systematically exceeded the experimental values. Similar observations have been made in the literature^[11].

4.2. Simulation results

The multiscale transport equations (5,9–11), the strain equation (15), and the viscoelastic stress equation (14)

were solved to simulate the moisture profiles, strain, and stress distributions for continuous drying and the fan on/off strategy at 40°C, 60°C, and 80°C. The aim was to examine the effectiveness of the fan on/off strategy with respect to drying time, energy consumption, and stress gradients. The slowest and fastest computation times were achieved for continuous drying at 80°C and intermittent drying at 40°C, respectively. The fastest computation time was 3 min and 17 s, while the slowest was 12 min and 12 s. The stress simulation results were also compared to experimental values of the global crack index to verify if conditions that minimize stress gradients in the bananas translate experimentally into lower stress cracking. In the model, the fan-off period was calculated by decreasing the air velocity to 0.01 m/s, while the temperature was kept constant.

4.2.1. Energy consumption and drying duration for continuous drying and the fan on/off strategy

The energy consumed during drying was calculated using:

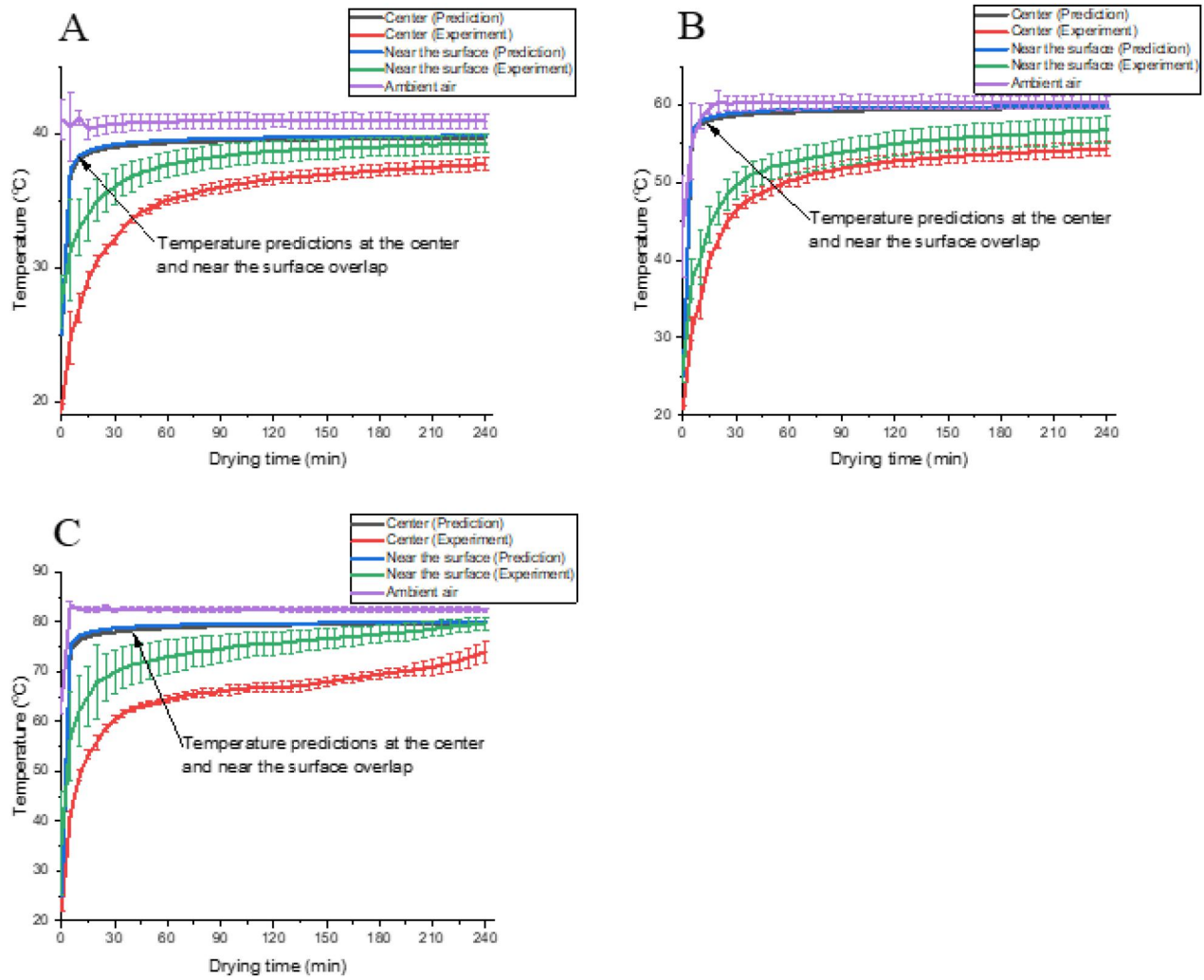


Figure 5. Comparison of predicted and experimental temperature distributions of bananas dried at A) 40°C and 20% RH, B) 60°C and 20% RH, and C) 80°C and 20% RH. Error bars indicate standard errors ($n = 4$).

$$Q_T = h_T(T_{amb} - T_{surf}) + h_m(\rho_{surf}^v - \rho_{amb}^v)\Delta H_v \quad (32)$$

where Q_T is the sum of the energy penetrating the material $h_T(T_{amb} - T_{surf})$, and the energy used for moisture evaporation in the boundary film $h_m(\rho_{surf}^v - \rho_{amb}^v)\Delta H_v$, h_T is the heat transfer coefficient, T_{amb} is the temperature of the ambient air, T_{surf} is the temperature at the surface, h_m is the moisture transfer coefficient, ρ_{amb}^v is the vapor density of ambient air, ρ_{surf}^v is the vapor density at the surface, and ΔH_v is the enthalpy of vaporization of water. Thus, the energy consumed up to a given drying time (t) can be determined by integrating Q_T over the external boundaries B and over time t as shown in (33).

$$E(t) = \int_0^t \int_B Q_T ds d\tau \quad (33)$$

Figure 6 presents the average moisture contents of banana simulated for continuous drying and the fan on/off strategy at 40°C, 60°C, and 80°C, while Figure 7 displays the corresponding energy consumed by the banana slice. A terminal moisture content of 17.1 g/g solids was selected based on indications by Mahomud et al.^[53] regarding the shelf life of banana slices.

Figure 6 illustrates that the fan on/off strategy results in 9–34% longer drying time compared to continuous drying. This percentage decreases with increasing temperature. Longer drying times with the fan on/off strategy also led to higher energy consumption, as shown in Figure 7. The additional energy consumed, in comparison to continuous drying, is 0.99%, 1.76%, and 3.08% at 40°C, 60°C, and 80°C, respectively. Many experimental studies using on/off intermittency have reported shorter effective drying times and energy savings^[54–57]. However,

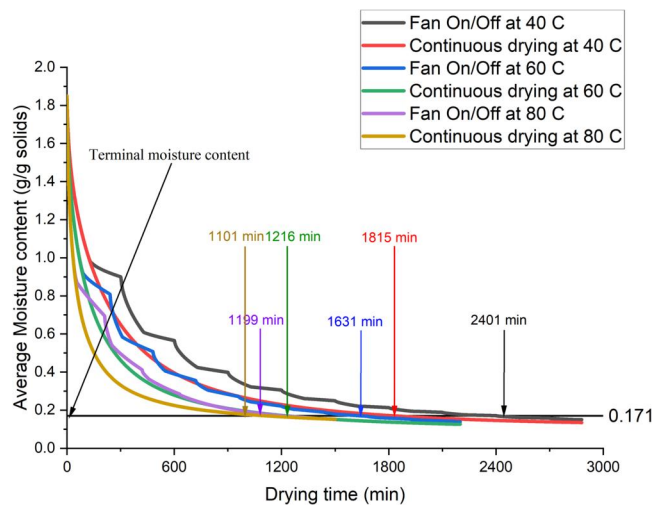


Figure 6. Simulated average moisture content for different drying strategies.

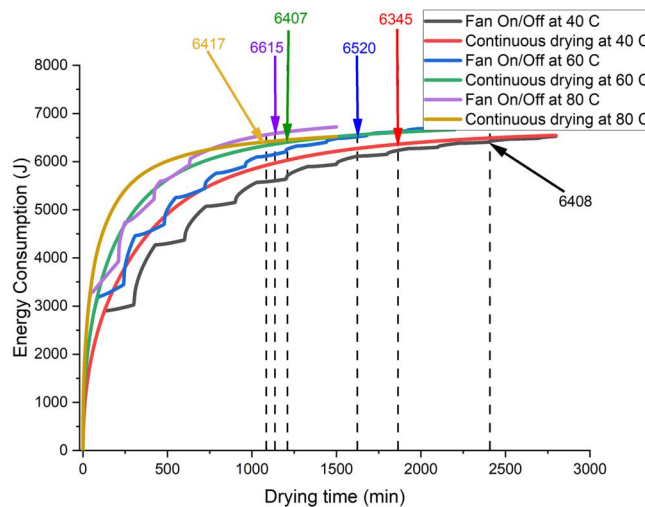


Figure 7. Simulated energy supplied to banana slices across different drying strategies.

the apparent contradiction can be explained by the type of intermittent run: the heat source was turned off in these experimental studies, whereas, in this study, only the fan was turned off. The increase in energy consumption (0.99–3.08%) when turning the fan on and off is modest compared to the magnitude of energy saving (19–52%) reported in the literature when turning the heat source on and off^[57]. Nevertheless, in practical processing operations, the cost of supplying 3.08% more energy, as calculated for the fan on/off strategy at 80 °C, compared to continuous drying at the same temperature, can be significant. Therefore, considering both energy consumption and drying time, the fan on/off strategy at 60 °C is preferable.

4.2.2. Moisture and strain profiles for continuous drying and the fan on/off strategy

Figure 8(A–F) show the distribution of moisture and strain in a banana slice along the axial direction, as

indicated in the inset. These figures also illustrate the moisture profile beneath the surface during continuous drying at 80 °C, and the fan on/off strategy. The plots in Figure 8(A,B) demonstrate a continuous decrease in moisture content and volumetric strain for all layers during continuous drying. This is expected to result in a non-uniform moisture distribution and, consequently, high-stress gradients in the banana slice. In contrast, when employing the fan on/off strategy, the moisture content of some external layers increased during the fan-off period (Figure 8(D)). Consequently, these layers expanded, as illustrated by the dashed rectangles in Figure 8(E). This increase in the moisture content within the external layers is expected to mitigate the moisture and stress gradients between the layers of bananas dried by intermittently turning the fan on and off. Therefore, samples subjected to this drying method are anticipated to be less susceptible to stress-cracking compared to those dried continuously.

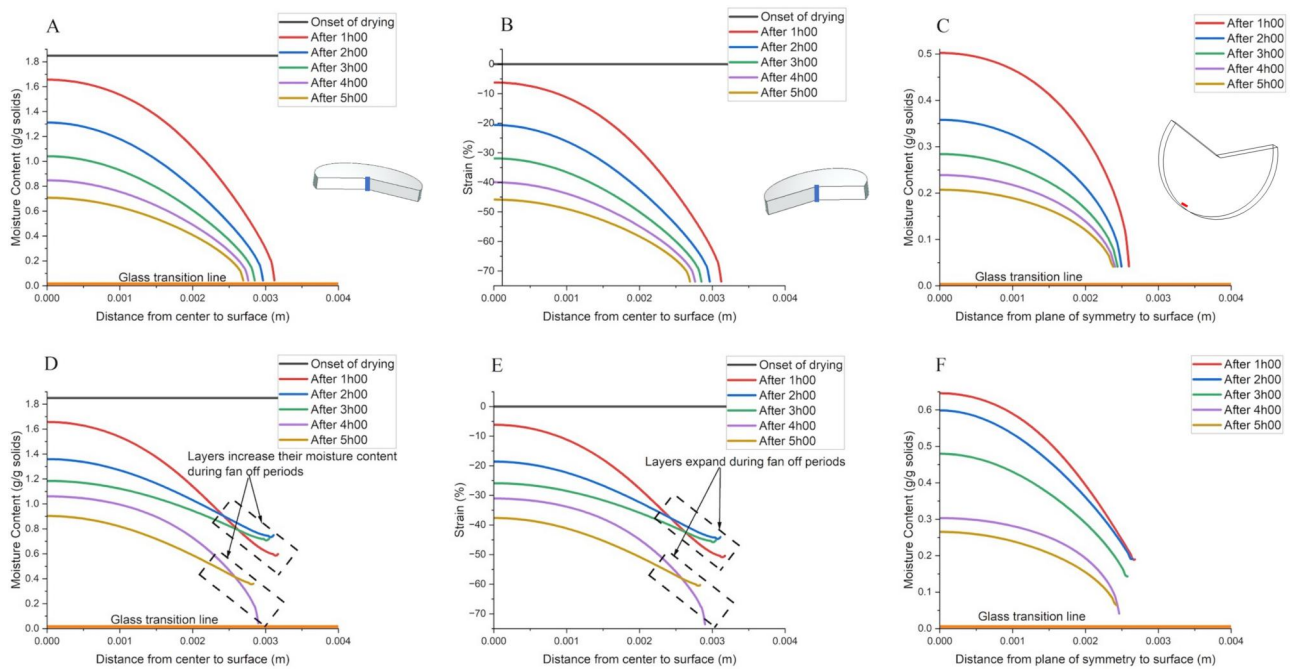


Figure 8. Profiles of moisture (a and D) and strain (B and E) along the axial direction and moisture profile beneath the surface (C and F) for banana slices under continuous drying and fan on/off drying at 80°C. Curves are plotted at 60-min intervals.

The plots in Figure 8(C,F) suggest that layers beneath the surface of the banana slice, as shown in the inset, were rubbery during the initial stage of drying. Subsequently, throughout the drying process, these regions approached glass transition due to the reduction in the moisture content. However, they did not cross the glass transition line.

These results are consistent with the findings reported by Abedi and Takhar^[40], who measured rheological properties of bananas and observed a continuous softening of ripe bananas during drying. The bananas used in this modeling study had a similar degree of ripeness (see Section 3.1.1). By measuring the relaxation modulus of ripe bananas at various moisture content levels, ranging from 1.8 g/g solids to 0.17 g/g solids, the researchers noted a decrease in modulus values as the moisture content decreased. This suggested that the ripe bananas did not undergo a glass transition during drying, as the relaxation modulus of a material in the glassy state is expected to be higher than in the rubbery state.

The authors explained this behavior by attributing it to the plasticizing effect of simple sugars generated through the hydrolysis of starch, pectin, and hemicellulose during the ripening process. Throughout the drying process, the plasticizing effect of these simple sugars, present in the bananas, compensated for the reduction in the plasticizing effect of water. As a result, the mobility of polymers was maintained, and the entire banana remained in the rubbery state.

Furthermore, no experimental evidence of case-hardening, which is associated with the transition from a rubbery to a glassy state of the outer layers^[58], was observed within the moisture content ranges used in this study. The transition from the rubbery to the glassy state and vice versa is also linked with stress cracking during the drying of food materials^[59]. Consequently, the drying of ripe bananas resulted in soft materials that were less prone to cracking caused by the glass transition.

4.2.3. Stress profiles for continuous drying and the fan on/off strategy

Figure 9 illustrates the simulated stress profiles along the axial direction for banana slices dried under continuous drying conditions and the fan on/off strategy at 40 °C, 60 °C, and 80 °C. The stress profiles are plotted at 3-h intervals for the first 24 h of drying.

The results presented in Figure 9 demonstrate that the stress magnitude increased with higher drying temperatures, longer drying times, and from the internal to outer layers of the banana slice. For example, after 24 h of continuous drying at 80 °C, the stress exceeded 11 kPa at the center, whereas it remained below 10 kPa at 40 °C.

Furthermore, Figure 9 also highlights that, for the same drying temperature and duration, the stress magnitudes were lower for the fan on/off strategy compared to continuous drying. For instance, after 6 h of drying at 40 °C, the stress at the center slightly

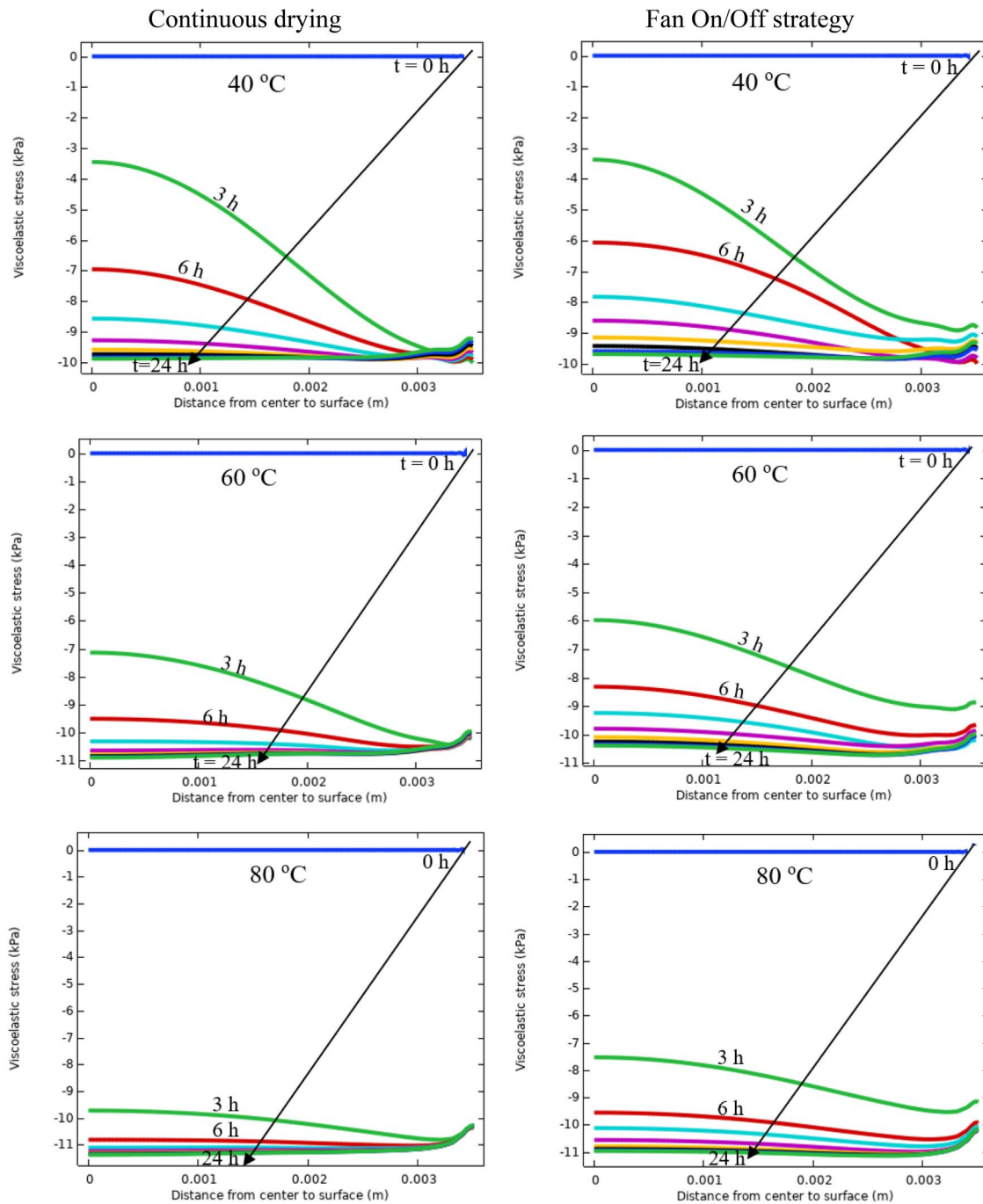


Figure 9. Stress distribution in a banana slice along the axial direction for various drying strategies.

exceeded 7 kPa for continuous drying, whereas it remained below 6 kPa for the fan on/off strategy. This reduction in stress magnitudes observed in the fan on/off strategy compared to continuous drying can be attributed to the resting periods, which helped to alleviate stress accumulation within the material^[57].

The accumulation of high stress within the material during drying can lead to stress cracking if it exceeds the material's ultimate strength. Therefore, banana slices dried continuously are more likely to experience cracking due to higher stress magnitudes compared to

slices dried at similar temperatures but with intermittent fan operation, where the fan is turned on and off intermittently.

4.2.4. Global crack index and stress profiles for continuous drying and the fan on/off strategy

To evaluate the overall effect of the intermittent air velocity on the development of cracks, sets of 30 banana slices were dried continuously at 40 °C, 60 °C, and 80 °C. Other groups were dried at the same temperatures but using the fan on/off strategy. Additional

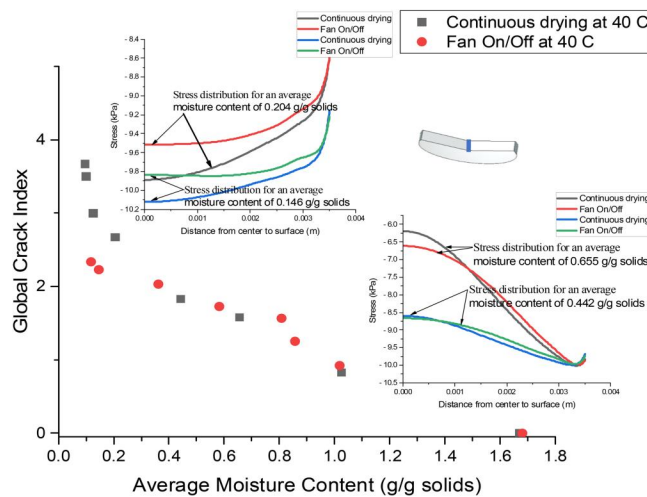


Figure 10. Global crack index and stress along the axial direction across drying strategies at 40°C.

sets of bananas were dried alongside for moisture content measurement. The global crack index was evaluated following the methodology described in Section 3.1.5 and related to the drying conditions and the average moisture content.

Continuous drying and the fan on/off strategy were also simulated using the model with the same drying conditions and identical fan on/off intervals used during the drying experiments. The stress profiles along the axial direction corresponding to the average moisture contents measured experimentally were then extracted during the post-processing of the simulation results.

Figures 10–12 show the global crack indices for continuous drying and the fan on/off strategy at 40°C, 60°C, and 80°C. For each temperature, two stress profiles are embedded into the graph. The stress profiles displayed correspond to two distinct regions—a region of low moisture content, which brackets the terminal moisture content of 0.171 g/g solids, and another in the intermediate moisture content range.

Figure 10 shows the global crack index for continuous drying and the fan on/off strategy at 40°C. Two stress profiles are displayed, which correspond to the average moisture contents of 0.655 and 0.442 g/g solids for the intermediate moisture content region and 0.204 and 0.146 g/g solids for the low moisture content region. Figure 10 reveals that the global crack indices of continuous drying and fan on/off strategy were comparable for a large part of the drying. Above 0.40 g/g solids, no significant difference existed.

The stress profiles at 0.655 and 0.442 g/g solids support this observation. The stress gradients induced by continuous drying are only moderately higher than those generated by the fan on/off strategy. However, at 0.204 g/g solids, stress gradients became significantly higher for continuous drying compared to the

fan on/off strategy. The global crack indices followed the same trend. The global crack index for the fan on/off strategy remained below 2.5, while its value for continuous drying exceeded 3.5. At a moisture content of 0.146 g/g solids, which is below the terminal value, the stress gradients for the fan on/off strategy remained less than those calculated for continuous drying. However, this difference diminished as the moisture content decreased. Therefore, drying bananas below the terminal moisture content using the fan on/off strategy could increase stress cracking.

Figure 11 shows the global crack index for the continuous drying and the fan on/off strategy at 60°C. The global crack index for the fan on/off strategy always remains below the values for continuous drying. This trend is also confirmed by the stress profiles along the axial direction. For the intermediate average moisture content range, the stress gradient at 0.64 g/g solids for the continuous drying was significantly higher than the stress gradient for the fan on/off strategy. This was also true at an average moisture content of 0.44 g/g solids.

Figure 12 presents the global crack index for continuous drying and the fan on/off strategy at 80°C. The axial stress profiles for continuous drying and the fan on/off strategy at 0.43, 0.29, 0.18, and 0.16 g/g solids are embedded in the figure. Figure 12 shows that global crack indices of continuous drying and the fan on/off strategy differed from an early drying stage. Continuous drying resulted in a high global crack index, while the index remained relatively low for the fan on/off strategy. The axial stress profiles agree with the experimental results. At 0.43 and 0.29 g/g solids average moisture contents, the axial stress gradients for continuous drying were significantly higher than for the fan on/off strategy. Thus, as hypothesized,

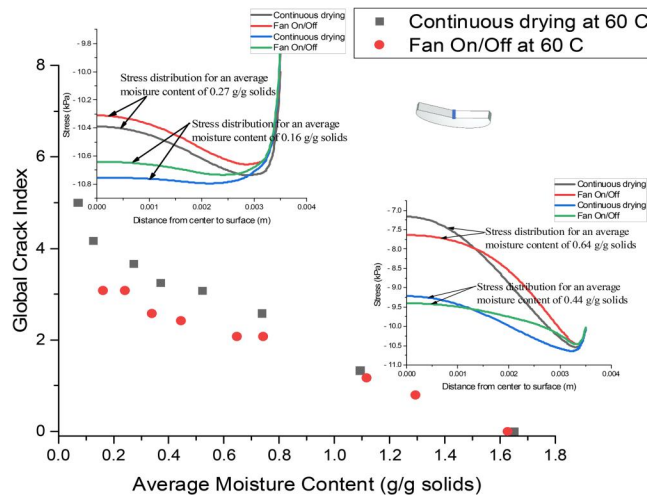


Figure 11. Global crack index and stress along the axial direction across drying strategies at 60°C.

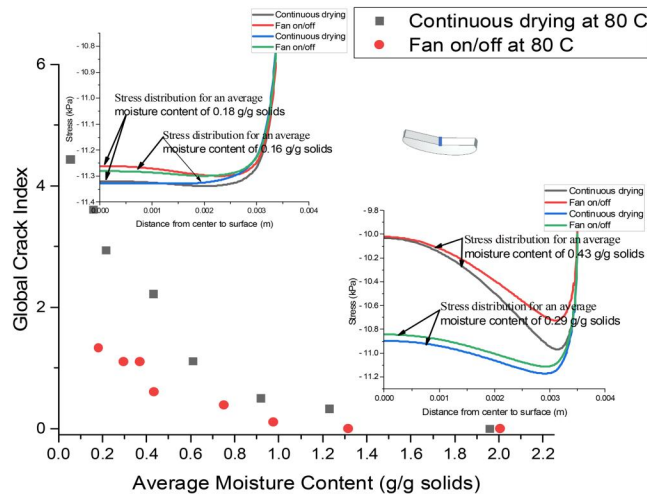


Figure 12. Global crack index and stress along the axial direction across drying strategies at 80°C.

stress gradient differences translated into significant differences in stress-cracking behavior.

At low moisture content, the axial stress gradient for the fan on/off strategy became slightly more pronounced than for the continuous drying. This could induce rapid crack development in bananas during the late drying stages using the fan on/off strategy.

Collectively, from Figures 10–12, it is evident that the difference in the axial stress gradients evaluated at the same average moisture content for samples dried differently is a good predictor of their likelihood to form stress cracks.

5. Conclusions

A model based on HMT was developed to investigate the mechanisms of transport, strain, and stress during banana convective drying. The banana was treated as a saturated, two-phase, multiscale system consisting of

water and a solid matrix. The transport model comprised coupled two-scale balance equations for mass, momentum, and energy. The viscoelastic stress equation complemented these transport equations. The model had the capability to predict both the Fickian and non-Fickian transport behaviors, especially when the material was near its glass transition.

Water movement inside the banana slices was primarily driven by the concentration gradients, and heat was transferred through a combination of conduction and convection. A phase change was implemented at the interface between banana and the ambient air. The effect of deformation on transport was accounted for by transforming the equations from Eulerian to Lagrangian coordinates.

The model allowed the prediction of the spatiotemporal distribution of water, temperature, strain, and viscoelastic stress. Its validity was established by comparing the average moisture content, the average

volumetric strain, the center temperature, and near-the-surface temperature with values determined experimentally (MAEs of 0.022–0.121 g/g solids for the moisture content, 0.06–0.13 for the volumetric strain, 2.1–7.7 °C for the temperature at the center, and MAEs of 0.6–3.2 °C for the near-the-surface temperature).

Subsequently, the model was employed to simulate various aspects of drying, including moisture profiles, energy consumption, strain profiles, and stress distribution during continuous drying and a fan on/off strategy at 40 °C, 60 °C, and 80 °C. By simulating stress profiles along the axial direction, it proved a viable approach to predict the likelihood of stress-crack formation in the material. As a result, intermittently turning the fan on/off during drying led to lower stress gradients at all temperatures compared to continuous drying, which was experimentally validated by observing lower values of the global crack index. However, the energy consumed by the banana during the fan on/off strategy was slightly higher due to the extended drying time compared to continuous drying.

The model developed in this study, and the simulation results obtained, can be applied to tune drying parameters to minimize strain and stress development in bananas. It also offers the opportunity to optimize between reducing the stress cracks and minimizing energy consumption in the drying process.

Latin symbols

A	Regression coefficient for calculating B_c , dimensionless
a_M	Moisture dependent shift factor, dimensionless
a_T	Temperature dependent shift factor, dimensionless
a_w	Water activity (decimal)
B	Regression coefficient for calculating B_c , dimensionless
B_c	Coefficient of the stress relaxation function, $m^3 s \text{ kg}^{-1}$
C_p^α	Specific heat of the α -phase, $\text{J kg}^{-1}\text{K}^{-1}$
d_i	Diameter at the drying time $t=0$ s, m
D^α	Diffusion coefficient of the α -phase, m^2s^{-1}
E	Energy consumed, J
E_{MM}	First invariant of the strain tensor, dimensionless
G_0	Elastic part of the relaxation function, Pa
G_m	Stress coefficient of the m th Maxwell element, Pa
$G(t)$	Relaxation function, Pa
h_m	Mass transfer coefficient, m s^{-1}
h_T	Heat transfer coefficient, $\text{W m}^{-2} \text{K}^{-1}$
j	Jacobian, dimensionless
k^α	Thermal conductivity of the α -phase, $\text{W m}^{-1}\text{K}^{-1}$
L	Characteristic length, m
M	Moisture content, g/g solids
M^w	Molecular weight of water, kg mol^{-1}
\bar{M}	Average moisture content, g/g solids
Nu	Nusselt number, dimensionless

P_{atm}	Atmospheric pressure, Pa
Pr	Prandtl number, dimensionless
P_{sat}	Saturated vapor pressure, Pa
P_{eq}^v	Pressure of the vapor phase at equilibrium, Pa
p^w	Partial pressure of water, Pa
Q_T	Heat flux, W m^{-2}
Q_v	Vapor flux, $\text{kg m}^{-2} \text{s}^{-1}$
Q_w	Water flux BC (see Table 4, +ve for influx, -ve for outflux), $\text{kg m}^{-2} \text{s}^{-1}$
REV	Representative elementary volume, m^3
Ru	Universal gas constant, $\text{J mol}^{-1}\text{K}^{-1}$
Re	Reynolds number, dimensionless
RH	Relative humidity, %
Sc	Schmidt number, dimensionless
Sh	Sherwood number, dimensionless
t	Time, s
T	Temperature, K
T_{amb}	Ambient air temperature, K
T_f	Film temperature, K
th_i	Initial thickness of the banana slice, m
v	Volume at the drying time t , m^3
V	Initial volume, m^3
$v^{w,s}$	Velocity of the water phase relative to the solid phase, m/s
v^α	Velocity of the α -phase (α =water, solid), ms^{-1}
x_j	j th experimental value, g/g solids or dimensionless or K
y_j	j th predicted value, g/g solids or dimensionless or K
Z_m	Viscoelastic stress of the m th Maxwell element, Pa

Greek symbols

ε^α	Volume fraction of the α -phase (α =water, solid), dimensionless
ρ^α	Density of the α -phase (α =water, solid), kg m^{-3}
λ_m	Relaxation time of the m th Maxwell element, s
λ'_m	Rescaled relaxation time of the m th Maxwell element, s
ΔH_v	Enthalpy of vaporization of water, J kg^{-1}
ζ	Displacement coefficient, dimensionless
σ	Stress tensor, Pa

Special symbols

dV	Eulerian volume of the material, m^3
dV	Lagrangian volume of the material, m^3
\hat{e}_r, \hat{e}_z	Unit vectors in Eulerian coordinates
LHS	Left-hand side
RHS	Right-hand side
∇_E	Spatial gradient in Eulerian coordinate, m^{-1}
∇_L	Spatial gradient in Lagrangian coordinate, m^{-1}
Dot (.)	Material time derivative following the motion of a solid particle, s^{-1}

Subscripts

0	Reference state
amb	Ambient
E	Eulerian coordinate
i	Initial
L	Lagrangian coordinate

Superscripts

g	Gas
s	Solid phase
v	Vapor phase
w	Water phase
α	General representation of a phase

Disclosure statement

The authors report there are no competing interests to declare.

Funding

This work was funded by the Center for Advanced Research in Drying (CARD) and the National Science Foundation (NSF) under the award number 1624812.

References

- [1] Siddiq, M.; Ahmed, J.; Lobo, M. G. *Handbook of Banana Production, Postharvest Science, Processing Technology, and Nutrition*; Wiley Online Library: Hoboken, NJ, 2020.
- [2] Prachayawarakorn, S.; Tia, W.; Plyto, N.; Soponronnarit, S. Drying Kinetics and Quality Attributes of Low-Fat Banana Slices Dried at High Temperature. *J. Food Eng.* **2008**, *85*, 509–517. DOI: [10.1016/j.jfoodeng.2007.08.011](https://doi.org/10.1016/j.jfoodeng.2007.08.011).
- [3] Takhar, P. S. Hybrid Mixture Theory Based Moisture Transport and Stress Development in Corn Kernels during Drying: Coupled Fluid Transport and Stress Equations. *J. Food Eng.* **2011**, *105*, 663–670. DOI: [10.1016/j.jfoodeng.2011.03.033](https://doi.org/10.1016/j.jfoodeng.2011.03.033).
- [4] Yang, W.; Jia, C.-C.; Siebenmorgen, T.; Pan, Z.; Cnossen, A. Relationship of Kernel Moisture Content Gradients and Glass Transition Temperatures to Head Rice Yield. *Biosyst. Eng.* **2003**, *85*, 467–476. DOI: [10.1016/S1537-5110\(03\)00091-6](https://doi.org/10.1016/S1537-5110(03)00091-6).
- [5] Arora, V.; Henderson, S.; Burkhardt, T. Rice Drying Cracking versus Thermal and Mechanical Properties. *Trans. ASAE* **1973**, *16*, 320–323. DOI: [10.13031/2013.37511](https://doi.org/10.13031/2013.37511).
- [6] Defraeye, T. Advanced Computational Modelling for Drying Processes—a Review. *Appl. Energy* **2014**, *131*, 323–344. DOI: [10.1016/j.apenergy.2014.06.027](https://doi.org/10.1016/j.apenergy.2014.06.027).
- [7] Katekawa, M.; Silva, M. A Review of Drying Models Including Shrinkage Effects. *Dry. Technol.* **2006**, *24*, 5–20. DOI: [10.1080/07373930500538519](https://doi.org/10.1080/07373930500538519).
- [8] Mahiuddin, M.; Khan, M. I. H.; Kumar, C.; Rahman, M. M.; Karim, M. Shrinkage of Food Materials during Drying: Current Status and Challenges. *Comp. Rev. Food Sci. Food Saf.* **2018**, *17*, 1113–1126. DOI: [10.1111/1541-4337.12375](https://doi.org/10.1111/1541-4337.12375).
- [9] Mayor, L.; Sereno, A. Modelling Shrinkage during Convective Drying of Food Materials: A Review. *J. Food Eng.* **2004**, *61*, 373–386. DOI: [10.1016/S0260-8774\(03\)00144-4](https://doi.org/10.1016/S0260-8774(03)00144-4).
- [10] Purlis, E.; Cevoli, C.; Fabbri, A. Modelling Volume Change and Deformation in Food Products/Processes: An Overview. *Foods* **2021**, *10*, 778. DOI: [10.3390/foods10040778](https://doi.org/10.3390/foods10040778).
- [11] Rahman, M. M.; Joardder, M. U.; Khan, M. I. H.; Pham, N. D.; Karim, M. Multi-Scale Model of Food Drying: Current Status and Challenges. *Crit. Rev. Food Sci. Nutr.* **2018**, *58*, 858–876. DOI: [10.1080/10408398.2016.1227299](https://doi.org/10.1080/10408398.2016.1227299).
- [12] Queiroz, M.; Nebra, S. Theoretical and Experimental Analysis of the Drying Kinetics of Bananas. *J. Food Eng.* **2001**, *47*, 127–132. DOI: [10.1016/S0260-8774\(00\)00108-4](https://doi.org/10.1016/S0260-8774(00)00108-4).
- [13] Johnson, P. T.; Brennan, J.; Addo-Yobo, F. Air-Drying Characteristics of Plantain (*Musa AAB*). *J. Food Eng.* **1998**, *37*, 233–242. DOI: [10.1016/S0260-8774\(98\)00076-4](https://doi.org/10.1016/S0260-8774(98)00076-4).
- [14] Jannot, Y.; Talla, A.; Nganhou, J.; Puiggali, J.-R. Modeling of Banana Convective Drying by the Drying Characteristic Curve (DCC) Method. *Dry. Technol.* **2004**, *22*, 1949–1968. DOI: [10.1081/DRT-200032888](https://doi.org/10.1081/DRT-200032888).
- [15] Dandamrongrak, R.; Young, G.; Mason, R. Evaluation of Various Pre-Treatments for the Dehydration of Banana and Selection of Suitable Drying Models. *J. Food Eng.* **2002**, *55*, 139–146. DOI: [10.1016/S0260-8774\(02\)00028-6](https://doi.org/10.1016/S0260-8774(02)00028-6).
- [16] Karim, M. A.; Hawlader, M. Drying Characteristics of Banana: Theoretical Modelling and Experimental Validation. *J. Food Eng.* **2005**, *70*, 35–45. DOI: [10.1016/j.jfoodeng.2004.09.010](https://doi.org/10.1016/j.jfoodeng.2004.09.010).
- [17] Bains, R.; Langrish, T. Choosing an Appropriate Drying Model for Intermittent and Continuous Drying of Bananas. *J. Food Eng.* **2007**, *79*, 330–343. DOI: [10.1016/j.jfoodeng.2006.01.068](https://doi.org/10.1016/j.jfoodeng.2006.01.068).
- [18] Seyedabadi, E.; Khojastehpour, M.; Abbaspour-Fard, M. H. Convective Drying Simulation of Banana Slabs considering Non-Isotropic Shrinkage Using FEM with the Arbitrary Lagrangian–Eulerian Method. *Int. J. Food Prop.* **2017**, *20*, S36–S49. DOI: [10.1080/10942912.2017.1288134](https://doi.org/10.1080/10942912.2017.1288134).
- [19] da Silva, W. P.; Rodrigues, A. F.; e Silva, C. M. D.; de Castro, D. S.; Gomes, J. P. Comparison between Continuous and Intermittent Drying of Whole Bananas Using Empirical and Diffusion Models to Describe the Processes. *J. Food Eng.* **2015**, *166*, 230–236. DOI: [10.1016/j.jfoodeng.2015.06.018](https://doi.org/10.1016/j.jfoodeng.2015.06.018).
- [20] Ranjan, R.; Irudayaraj, J.; Reddy, J.; Mujumdar, A. Finite-Element Simulation and Validation of Stepwise Drying of Bananas. *Numer. Heat Transf. A* **2004**, *45*, 997–1012. DOI: [10.1080/10407780490453963](https://doi.org/10.1080/10407780490453963).
- [21] Davila, R. F. Z. *Mathematical Modeling of Drying Process of Unripe Banana Slices*; Universidade de São Paulo: São Paulo, Brazil, 2016.
- [22] Caballero-Cerón, C.; Serment-Moreno, V.; Velazquez, G.; Torres, J. A.; Welti-Chanes, J. Hygroscopic Properties and Glass Transition of Dehydrated Mango, Apple and Banana. *J. Food Sci. Technol.* **2018**, *55*, 540–549. DOI: [10.1007/s13197-017-2963-3](https://doi.org/10.1007/s13197-017-2963-3).
- [23] Battiato, I.; Ferrero V, P. T.; O' Malley, D.; Miller, C. T.; Takhar, P. S.; Valdés-Parada, F. J.; Wood, B. D. Theory and Applications of Macroscale Models

- in Porous Media. *Trans. Porous Med.* **2019**, *130*, 5–76. DOI: [10.1007/s11242-019-01282-2](https://doi.org/10.1007/s11242-019-01282-2).
- [24] Takhar, P. S. Unsaturated Fluid Transport in Swelling Poroviscoelastic Biopolymers. *Chem. Eng. Sci.* **2014**, *109*, 98–110. DOI: [10.1016/j.ces.2014.01.016](https://doi.org/10.1016/j.ces.2014.01.016).
- [25] De Vries, D. Simultaneous Transfer of Heat and Moisture in Porous Media. *Eos, Trans. Am. Geophys. Union* **1958**, *39*, 909–916. DOI: [10.1029/TR039i005p00909](https://doi.org/10.1029/TR039i005p00909).
- [26] Singh, P. P.; Cushman, J. H.; Maier, D. E. Three Scale Thermomechanical Theory for Swelling Biopolymeric Systems. *Chem. Eng. Sci.* **2003**, *58*, 4017–4035. DOI: [10.1016/S0009-2509\(03\)00283-5](https://doi.org/10.1016/S0009-2509(03)00283-5).
- [27] Ozturk, O. K.; Takhar, P. S. Hybrid Mixture Theory-Based Modeling of Moisture Transport Coupled with Quality Changes in Strawberries and Carrots. *Dry. Technol.* **2021**, *39*, 932–949. DOI: [10.1080/07373937.2020.1733005](https://doi.org/10.1080/07373937.2020.1733005).
- [28] Eringen, A. C. *Mechanics of Continua*. Huntington; R.E. Krieger Pub. Co.: Huntington, NY, 1980.
- [29] Ditudompo, S.; Takhar, P. S. Hybrid Mixture Theory Based Modeling of Transport Mechanisms and Expansion-Thermomechanics of Starch during Extrusion. *AIChE. J.* **2015**, *61*, 4517–4532. DOI: [10.1002/aic.14936](https://doi.org/10.1002/aic.14936).
- [30] Bennethum, L. S.; Cushman, J. H. Multiscale, Hybrid Mixture Theory for Swelling Systems—I: Balance Laws. *Int. J. Eng. Sci.* **1996**, *34*, 125–145. DOI: [10.1016/0020-7225\(95\)00089-5](https://doi.org/10.1016/0020-7225(95)00089-5).
- [31] Poling, B. E.; Prausnitz, J. M.; O'connell, J. P. *Properties of Gases and Liquids*; McGraw-Hill Education: New York, NY, **2001**.
- [32] Bart-Plange, A.; Addo, A.; Ofori, H.; Asare, V. Thermal Properties of Gros Michel Banana Grown in Ghana. *ARNP J. Eng. Appl. Sci.* **2012**, *7*, 478–484. https://www.arnpjournals.com/jeas/research_papers/rp_2012/jeas_0412_679.pdf.
- [33] Záborský, M.; Růžička, V.Jr. Domalski, E. S. Heat Capacity of Liquids: Critical Review and Recommended Values. Supplement I. *J. Phys. Chem. Ref. Data* **2001**, *30*, 1199–1689. DOI: [10.1063/1.1407866](https://doi.org/10.1063/1.1407866).
- [34] Vargaftik, N. B. *Tables on the Thermophysical Properties of Liquids and Gases*; Hemisphere Pub. Corp.: Washington, DC, **1975**.
- [35] Ajibola, O. Desorption Isotherms for Plantain at Several Temperatures. *J. Food Sci.* **1986**, *51*, 169–171. DOI: [10.1111/j.1365-2621.1986.tb10862.x](https://doi.org/10.1111/j.1365-2621.1986.tb10862.x).
- [36] Singh, P. P.; Maier, D. E.; Cushman, J. H.; Campanella, O. H. Effect of Viscoelastic Relaxation on Moisture Transport in Foods. Part II: Sorption and Drying of Soybeans. *J. Math. Biol.* **2004**, *49*, 20–34. DOI: [10.1007/s00285-003-0250-6](https://doi.org/10.1007/s00285-003-0250-6).
- [37] Knauss, W. G.; Emri, I. Volume Change and the Nonlinearly Thermo-Viscoelastic Constitution of Polymers. *Polym. Eng. Sci.* **1987**, *27*, 86–100. DOI: [10.1002/pen.760270113](https://doi.org/10.1002/pen.760270113).
- [38] Dlubek, G.; Kilburn, D.; Bondarenko, V.; Pionteck, J.; Krause-Rehberg, R.; Alam, M. Characterisation of Free Volume in Amorphous Materials by PALS in Relation to Relaxation Phenomena. Presented at the 24th Arbeitskreisstagung 'Nichtkristalline Strukturen' of DGK, Jena, Germany, September **2003**.
- [39] Wästlund, C.; Maurer, F. H. Positron Lifetime Distributions and Free Volume Parameters of PEO/PMMA Blends Determined with the Maximum Entropy Method. *Macromolecules* **1997**, *30*, 5870–5876. DOI: [10.1021/ma961604j](https://doi.org/10.1021/ma961604j).
- [40] Abedi, F. M.; Takhar, P. S. Stress Relaxation Properties of Bananas during Drying. *J. Texture Stud.* **2022**, *53*, 146–156. DOI: [10.1111/jtxs.12637](https://doi.org/10.1111/jtxs.12637).
- [41] Hammerle, J.; Mohsenin, N. Tensile Relaxation Modulus of Corn Horny Endosperm as a Function of Time, Temperature and Moisture Content. *Trans. ASAE* **1970**, *13*, 372–0375. DOI: [10.13031/2013.38612](https://doi.org/10.13031/2013.38612).
- [42] Green, D.; Southard, M. *Perry's Chemical Engineering Handbook*, 9th ed.; McGraw-Hill Publishing: New York, NY, **2019**.
- [43] Cengel, Y. A.; Boles, M. A.; Kanoglu, M. *Thermodynamics: An Engineering Approach*; McGraw-Hill Education: New York, NY, **2015**.
- [44] Nellis, G.; Klein, S. *Mass Transfer. Heat Transfer*; Cambridge University Press, New York, NY, **2009**.
- [45] Bergman, T. L.; Bergman, T. L.; Incropera, F. P.; Dewitt, D. P.; Lavine, A. S. *Fundamentals of Heat and Mass Transfer*; John Wiley & Sons: Hoboken, NJ, **2011**.
- [46] Mendoza, F.; Aguilera, J.; Dejmek, P. Predicting Ripening Stages of Bananas (*Musa Cavendish*) by Computer Vision. Presented at the V International Postharvest Symposium, Verona, Italy, June 30, **2004**; pp. 1363–1370. DOI: [10.17660/ActaHortic.2005.682.183](https://doi.org/10.17660/ActaHortic.2005.682.183).
- [47] AACC. AACC Method 44-15.02 Moisture—Air-Oven Methods. In *AACC Approved Methods of Analysis*; AACC: Washington, DC, **1999**.
- [48] Willmott, C. J.; Matsuura, K. Advantages of the Mean Absolute Error (MAE) over the Root Mean Square Error (RMSE) in Assessing Average Model Performance. *Clim. Res.* **2005**, *30*, 79–82. DOI: [10.3354/cr030079](https://doi.org/10.3354/cr030079).
- [49] Giner, S. A. Influence of Internal and External Resistances to Mass Transfer on the Constant Drying Rate Period in High-Moisture Foods. *Biosyst. Eng.* **2009**, *102*, 90–94. DOI: [10.1016/j.biosystemseng.2008.09.022](https://doi.org/10.1016/j.biosystemseng.2008.09.022).
- [50] Marousis, S.; Karathanos, V.; Saravacos, G. Effect of Sugars on the Water Diffusivity in Hydrated Granular Starches. *J. Food Sci.* **1989**, *54*, 1496–1552. DOI: [10.1111/j.1365-2621.1989.tb05144.x](https://doi.org/10.1111/j.1365-2621.1989.tb05144.x).
- [51] Leslie, R.; Carillo, P.; Chung, T.; Gilbert, S.; Hayakawa, K.; Marousis, S.; Saravacos, G.; Solberg, M. Water Diffusivity in Starch-Based Systems. In *Water Relationships in Foods*; Springer: Berlin, Germany, **1991**; pp. 365–390.
- [52] Saravacos, G.; Karathanos, V.; Marousis, S. Diffusion of Water in Starch Materials. In *Developments in Food Science*; Elsevier: Amsterdam, Netherlands, **1992**; Vol. 29, pp. 329–340.
- [53] Mahomud, M. S.; Ali, M. K.; Rahman, M. M.; Rahman, M. H.; Sharmin, T.; Rahman, M. J. Effect of Honey and Sugar Solution on the Shelf Life and

- Quality of Dried Banana (*Musa Paradisiaca*) Slices. *Am. J. Food Sci. Technol.* **2015**, 3(3), 60–66. DOI: [10.12691/ajfst-3-3-2](https://doi.org/10.12691/ajfst-3-3-2).
- [54] Chin, S. K.; Law, C. L. Product Quality and Drying Characteristics of Intermittent Heat Pump Drying of *Ganoderma Tsugae* Murrill. *Dry. Technol.* **2010**, 28, 1457–1465. DOI: [10.1080/07373937.2010.482707](https://doi.org/10.1080/07373937.2010.482707).
- [55] Yang, Z.; Zhu, E.; Zhu, Z.; Wang, J.; Li, S. A Comparative Study on Intermittent Heat Pump Drying Process of Chinese Cabbage (*Brassica Campestris* L. ssp) Seeds. *Food Bioprod. Process.* **2013**, 91, 381–388. DOI: [10.1016/j.fbp.2013.02.006](https://doi.org/10.1016/j.fbp.2013.02.006).
- [56] Pan, Y.; Zhao, L.; Hu, W. The Effect of Tempering-Intermittent Drying on Quality and Energy of Plant Materials. *Dry. Technol.* **1998**, 17, 1795–1812. DOI: [10.1080/07373939908917653](https://doi.org/10.1080/07373939908917653).
- [57] Kumar, C.; Karim, M.; Joardder, M. U. Intermittent Drying of Food Products: A Critical Review. *J. Food Eng.* **2014**, 121, 48–57. DOI: [10.1016/j.jfoodeng.2013.08.014](https://doi.org/10.1016/j.jfoodeng.2013.08.014).
- [58] Gulati, T.; Datta, A. K. Mechanistic Understanding of Case-Hardening and Texture Development during Drying of Food Materials. *J. Food Eng.* **2015**, 166, 119–138. DOI: [10.1016/j.jfoodeng.2015.05.031](https://doi.org/10.1016/j.jfoodeng.2015.05.031).
- [59] Gnossen, A.; Siebenmorgen, T. The Glass Transition Temperature Concept in Rice Drying and Tempering: Effect on Milling Quality. *Trans. ASAE* **2000**, 43, 1661. DOI: [10.13031/2013.3066](https://doi.org/10.13031/2013.3066).